



1 **Impacts of ice-nucleating particles from marine aerosols on mixed-phase orographic clouds**  
2 **during 2015 ACAPEX field campaign**

3

4 Yun Lin<sup>1,2</sup>, Jiwen Fan<sup>1,\*</sup>, Pengfei Li<sup>3,4</sup>, L. Ruby Leung<sup>1</sup>, Paul J. DeMott<sup>5</sup>, Lexie Goldberger<sup>1</sup>,  
5 Jennifer Comstock<sup>1</sup>, Ying Liu<sup>1</sup>, Jong-Hoon Jeong<sup>1,2</sup>, Jason Tomlinson<sup>1</sup>

6

7 <sup>1</sup> Atmospheric Sciences and Global Change Division, Pacific Northwest National Laboratory,  
8 Richland, WA 99352, USA

9 <sup>2</sup> Joint Institute for Regional Earth System Science and Engineering (JIFRESSE), University of  
10 California, Los Angeles (UCLA), Los Angeles, CA 90064, USA

11 <sup>3</sup> College of Science and Technology, Hebei Agricultural University, Baoding, Hebei  
12 14 071000, P.R. China

13 <sup>4</sup> Research Center for Air Pollution and Health; Key Laboratory of Environmental  
14 Remediation and Ecological Health, Ministry of Education, College of Environment and  
15 Resource Sciences, Zhejiang University, Hangzhou, Zhejiang 310058, P.R. China

16 <sup>5</sup> Department of Atmospheric Science, Colorado State University, Fort Collins, CO 80523, USA

17

18 Corresponding author: Jiwen Fan ([jiwen.fan@pnnl.gov](mailto:jiwen.fan@pnnl.gov))

19

20

21



22 **Abstract**

23 A large fraction of annual precipitation over the western United States comes from wintertime  
24 orographic clouds associated with atmospheric rivers (ARs). The transported African and Asian  
25 dust and marine aerosols from the Pacific Ocean may act as ice-nucleating particles (INPs) to  
26 affect cloud and precipitation properties over the region. Here we explored the effects of INPs  
27 from marine aerosols on orographic mixed-phase clouds and precipitation at different AR stages  
28 for an AR event observed during the 2015 ACAPEX field campaign under low dust ( $< 0.02 \text{ cm}^{-3}$ )  
29 conditions. Simulations were conducted using the chemistry version of the Weather Research  
30 and Forecasting model coupled with the spectral-bin microphysics at 1-km grid spacing, with ice  
31 nucleation connected with dust and marine aerosols. By comparing against airborne and ground-  
32 based observations, accounting for marine INP effects improves the simulation of cloud phase  
33 state and precipitation. The marine INPs enhance the formation of ice and snow, leading to less  
34 shallow warm clouds but more mixed-phase and deep clouds, and increased ice water path (over  
35 5 times) and snow precipitation (over 40 times). The responses of cloud and precipitation to  
36 marine INPs vary with the AR stages with more significant effects before AR landfall and post-  
37 AR than after AR landfall, mainly because the moisture and temperature conditions change with  
38 the AR evolution. This work suggests weather and climate models need to consider the impacts  
39 of marine INPs since their contribution is notable under low dust conditions despite the much  
40 lower relative ice nucleation efficiency of marine INPs.

41



## 42 **1 Introduction**

43 Atmospheric river (AR) events have great impacts on atmospheric and hydrological  
44 processes in the western United States during winter. They account for 30–50% of the total  
45 winter precipitation through their impacts on orographic clouds and associated heavy  
46 precipitation (Dettinger et al., 2011). Understanding the factors influencing different types of  
47 precipitation (rain vs. snow) associated with ARs is crucial for planning and managing regional  
48 water resources and hydrologic hazards and improving atmospheric and hydrologic forecasting  
49 in the western United States. Rain and snow precipitation produced by orographic clouds over  
50 the Sierra Nevada Mountains is closely related to the partitioning between cloud liquid and ice  
51 phases, which can be largely modified by aerosol particles (Rosenfeld et al., 2013; Fan et al.,  
52 2014, 2017b). However, aerosol-orography-precipitation relationships are complicated,  
53 depending on aerosol properties, mountain geometry, cloud phase, temperature, humidity, and  
54 flow patterns as reviewed in Chouldhury et al. (2019).

55 Over the western United States, understanding the roles of aerosols, particularly those  
56 capable of initiating ice crystal formation, in altering clouds and precipitation is still limited,  
57 which has motivated recent observational and modeling studies (Ault et al., 2011; Creamean et  
58 al., 2013, 2015; Rosenfeld et al., 2013; Fan et al., 2014, 2017b; Martin et al., 2019; Levin et al.,  
59 2019). While it has been found that long-range transported aerosols particularly dust particles as  
60 ice nucleating particles (INPs) influence clouds and precipitation in the mountainous western  
61 United States (Uno et al., 2009; Ault et al., 2011; Creamean et al., 2013), it is also clear from  
62 measurements that clouds occurring in and around ARs can also be influenced by INPs with  
63 apparent sources from the ocean (Levin et al., 2019).



64           Where sufficient INPs are present, heterogeneous ice nucleation can occur at a higher  
65   temperature where liquid and ice can co-exist, in contrast to homogeneous freezing which  
66   normally requires  $-38\text{ }^{\circ}\text{C}$  or colder environment (DeMott et al., 2010; Vali et al., 2015).  
67   Increasing INPs can lead to stronger ice formation and growth at the expense of supercooled  
68   liquid and increase precipitation. This concept is the basis of using cloud seeding to increase  
69   orographic precipitation (Reynolds, 1988; Geerts et al., 2010; French et al., 2018). For  
70   orographic clouds in the western United States, previous studies showed that INPs can increase  
71   total precipitation through the “seeder feeder” mechanism (Choulaton and Perry, 1986;  
72   Creamean et al., 2013), in which ice crystals that form in the upper portions of orographic clouds  
73   can collect droplets and grow to a larger size as they fall through a supercooled liquid layer  
74   before reaching the ground. Fan et al. (2014, 2017b) found that INPs like dust particles can  
75   increase precipitation by enhancing riming and deposition processes in mixed-phase orographic  
76   clouds, consistent with other studies (e.g., Muhlbauer and Lohmann, 2009; Xiao et al., 2015;  
77   Hazra et al., 2016; Yang et al., 2020). Fan et al. (2017a) also noted that the relative importance of  
78   riming to deposition depends on the mixed-phase cloud temperatures. Despite the importance of  
79   INPs in cloud formation and precipitation, they typically have a low abundance and large  
80   variations in their nucleating characteristics, especially in terms of the temperatures over which  
81   they initiate ice crystal formation (Kanji et al., 2017; Levin et al., 2019). Hence, there is large  
82   uncertainty in evaluating INPs impacts on mixed-phase and ice clouds as well as precipitation.

83           It is known that dust particles are important INP sources, which can initiate freezing over  
84   a range of temperatures but most efficiently below  $-20\text{ }^{\circ}\text{C}$  (Murray et al., 2012; Kanji et al.,  
85   2017). Another important type of INPs is terrestrially sourced biological particles, which cause  
86   freezing at temperatures as warm as  $-5\text{ }^{\circ}\text{C}$  (Murray et al., 2012). During ARs, the long-range



87 transport of dust or biological particles is highly episodic. Sea spray or marine aerosols  
88 consisting of sea salt and marine organic carbon resulting from wave breaking and bubble  
89 bursting at the ocean surface may also be a source of INPs (Burrows et al., 2013; Vergara-  
90 Temprado et al., 2017; McCluskey et al., 2018b; Levin et al., 2019). Recently, McCluskey et al.  
91 (2018a) derived an ice nucleation parameterization for INPs from sea spray aerosols based on  
92 observations collected at a North Atlantic coastal site and its relation to the marine aerosol  
93 surface area. Given the distinct physio-chemical characteristics and the different ice-nucleating  
94 efficiency, the impact of marine INPs on cloud and precipitation could be very different from  
95 dust or biological particles (DeMott et al., 2016; Kanji et al., 2017). However, studies of marine-  
96 sourced INP effects on clouds and associated precipitation are limited (Kanji et al., 2017; Levin  
97 et al., 2019). A few previous studies investigated the impacts of marine INPs on precipitation and  
98 radiation with global climate models (Hoose et al., 2010; Burrows et al., 2013; Yun and Penner,  
99 2013), albeit without the advantage of direct data on their ice nucleation efficiencies. Further, a  
100 detailed, process-level understanding of how marine INPs affect mixed-phase cloud processes  
101 and precipitation is lacking.

102       Following the CalWater campaigns in 2009, 2011, 2014, an interagency sponsored study,  
103 CalWater 2015, utilized a larger suite of instruments and measurement platforms to study ARs  
104 and aerosol-cloud interactions in AR environments (Ralph et al., 2016). As part of CalWater  
105 2015, the U.S. Department of Energy sponsored Atmospheric Radiation Measurement (ARM)  
106 Cloud Aerosol Precipitation Experiment (ACAPEX) field campaign aimed specifically at  
107 improving understanding and modeling of aerosol impacts on winter storms associated with  
108 landfalling ARs (Leung et al., 2016). The ACAPEX campaign conducted intensive sampling of  
109 clouds and aerosols using instruments on board the ARM Aerial Facility Gulfstream (G-1)



110 aircraft and ARM Mobile Facility on board the research vessel Ron Brown. These measurements  
111 were made in conjunction with clouds and aerosols, meteorological, hydrological, and oceanic  
112 measurements collected by instruments on three other aircraft and Ron Brown and at a coastal  
113 surface station. Collectively, these data provide a unique opportunity to examine the complex  
114 interactions among aerosols, orographic clouds, and ARs.

115 A major AR event spanning over 5 - 9 February 2015 occurred during the ACAPEX  
116 campaign and made landfall on the coast of Northern California, producing heavy rainfall with  
117 some regions receiving up to 400 mm of total precipitation during the event (Ralph et al., 2016;  
118 Cordeira et al., 2017). This AR event was extensively sampled by the (G-1 aircraft (Schmid et  
119 al., 2014) for characterizing aerosol and cloud properties. During this event, marine aerosols  
120 were the main aerosol type and marine INPs were dominant at cloud activation temperatures.  
121 Aerosol sampled by G-1 indicated that dust and biological particles were rather scarce in and  
122 around ARs, which is in stark contrast to the dominance of dust INPs during the AR events in the  
123 CalWater 2011 campaign (Levin et al., 2019). Therefore, the AR event during the ACAPEX  
124 campaign provides a rather unique opportunity to explore the role of marine aerosols in the  
125 orographic clouds and precipitation associated with landfalling ARs in the western United States.

126 In our previous modeling studies (Fan et al., 2014, 2017b), we implemented an  
127 immersion freezing parameterization for dust particles (DeMott et al. 2015) in a spectral-bin  
128 microphysics (SBM) scheme to examine the long-range dust effects on AR-associated  
129 orographic mixed-phase clouds and precipitation during CalWater 2011. With marine INPs  
130 dominating in CALWATER 2015/ACAPEX, in this study we implemented the recently  
131 developed ice immersion nucleation parameterization for sea spray aerosols by McCluskey et al.  
132 (2018b) in the SBM scheme. To explicitly simulate various aerosol types, different from Fan et



133 al. (2014, 2017a) who prescribed aerosols based on observations, a chemistry version of the  
134 Weather Research and Forecasting model (WRF-Chem) coupled with the SBM (Gao et al.,  
135 2016) was employed to predict aerosol properties and their interactions with clouds and radiation  
136 for the AR event on 6 - 9 February 2015. We focused on exploring the effects of INPs from sea  
137 spray aerosols, in competition with mineral dust INPs, on the orographic mixed-phase clouds and  
138 precipitation at different stages of the AR event as thermodynamic conditions evolved with the  
139 different AR stages.

## 140 **2 Model configuration and experiment design**

141 The WRF-Chem version 3.6 coupled with SBM as described in Gao et al. (2016) is  
142 employed for model simulations of this study, in which SBM is coupled with the Model for  
143 Simulating Aerosol Interactions and Chemistry (MOSAIC; Fast et al., 2006; Zaveri et al., 2008).  
144 The SBM scheme is a fast version in which ice crystal and snow (aggregates) in the full version  
145 are represented with a single size distribution (low-density ice) with a separation at 150  $\mu\text{m}$  in  
146 radius, with graupel or hail populating larger sizes (Khain et al., 2009, 2010; Fan et al., 2012,  
147 2017a). Here we choose the graupel version since hail is not one of the major cloud  
148 hydrometeors in the case we simulate. The WRF-Chem-SBM model is particularly designed to  
149 improve simulations of aerosol effects on clouds for complicated aerosol compositions and  
150 heterogeneous spatial distribution of aerosols. It has been applied in several studies including  
151 warm stratocumulus clouds (Gao et al., 2016), thunderstorms (Fan et al. 2020; Zhang et al.,  
152 2020), and supercell storms (Lin et al., 2020). Here WRF-Chem-SBM is employed, different  
153 from our previous studies in Fan et al. (2014, 2017a) which used WRF-SBM with prescribed  
154 aerosols, in order to explicitly simulate various aerosol types including marine aerosols and dust  
155 particles.



156 The four-sector MOSAIC aerosol module is chosen for the simulations of aerosols and  
157 the CBMZ (Carbon Bond Mechanism version Z) is used for gas-phase chemistry. The MOSAIC  
158 module treats nine major aerosol species (sulfate, nitrate, chloride, ammonium, sodium, black  
159 carbon, primary organics, other inorganics (OIN), and water). OIN is used as a surrogate of dust  
160 and the production of dust is parameterized with the dust transport model DUSTRAN (Shaw et  
161 al., 2008). Sea salt aerosol (the combination of sodium and chloride), as a surrogate for all SSA,  
162 is parameterized as a function of sea-surface wind speed (Gong et al., 1997b, a). The dry  
163 diameters of the particles over the four bins have a range of 0.039–0.156, 0.156–0.624, 0.624–  
164 2.5, and 2.5–10.0  $\mu\text{m}$ , respectively. For the total aerosol, aerosol size distribution over each  
165 section is represented with a 2-moment approach that predicts aerosol mass and number  
166 following a log-normal distribution [Simmel and Wurzler, 2006]. For each composition such as  
167 dust and sea salt, only the mass mixing ratio in each section is predicted and outputted. The  
168 aerosol number mixing ratio in each bin is only predicted for the total aerosol. Therefore, in this  
169 study, the dust and sea salt number mixing ratios used for ice nucleation parameterizations are  
170 derived based on their respective mass mixing ratio by assuming the same size and density of all  
171 particles over each bin, that is,

$$172 \quad N_{i,j} = \frac{m_j}{6\pi(D_j)^3 \rho_i}$$

173 where  $i$  denotes the aerosol composition (sea salt or dust here),  $j$  denotes the  $j^{\text{th}}$  aerosol bin,  $m_j$  is  
174 the total mass mixing ratio of the  $j^{\text{th}}$  bin,  $\rho_i$  is the assumed density (i.e., 2.6  $\text{g cm}^{-3}$  for dust and  
175 2.2 for sea salt), and  $D_j$  is the geometric mean diameter of the  $j^{\text{th}}$  bin. The approach for deriving  
176 the number mixing ratio for each aerosol component has been used in the literature (i.e., Zhao et  
177 al., 2013). We understand that the assumption that all particles have the same size over each bin





178 may introduce some uncertainty. However, the size distribution of each aerosol component is  
179 unknown in the model and any assumption on the size distribution might introduce uncertainty.

180

## 181 **2.1 Implementing an immersion freezing parameterization for marine INPs**

182 In the original SBM model, the ice nucleation accounting for both deposition ice  
183 nucleation and condensation-freezing is parameterized based on Meyers et al. (1992) and Bigg  
184 (1953) is employed for the immersion and homogeneous drop freezing. Neither of the ice  
185 nucleation parameterizations is connected with aerosols. Bigg (1953) was formulated based on  
186 the stochastic hypothesis where the freezing probability is assumed proportional to drop mass  
187 and the freezing rate is as a function of temperature without involving INPs. Fan et al. (2014,  
188 2017a) implemented DeMott et al. (2015) as an immersion freezing parameterization to  
189 investigate the effects of dust INPs on orographic mixed-phase clouds and precipitation during  
190 CalWater 2011. We adapted this implementation to WRF-Chem-SBM for this study to connect  
191 ice nucleation with dust particles. Developed based on both laboratory data and field  
192 measurements, DeMott et al. (2015) is an empirical parameterization for immersion freezing of  
193 natural mineral dust particles. INP concentrations are quantified as functions of temperature and  
194 the total number concentration of particles larger than 0.5  $\mu\text{m}$  diameter. In our implementation,  
195 the dust number mixing ratio for each aerosol bin is derived from its mass as detailed in the  
196 section above. The total dust number mixing ratio inputted to DeMott et al. (2015) is the  
197 integration over 0.5 -10  $\mu\text{m}$ .

198 To connect ice nucleation with sea spray aerosols, we implemented McCluskey et al.  
199 (2018a, thereafter MC2018), which was developed for quantifying ice nucleating activity by  
200 marine organics over the North Atlantic Ocean, in SBM following a similar approach as the  
201 implementation of DeMott et al. (2015). The nucleation site density in MC2018 is described as



202 
$$n_s = \exp(-0.545(T - 273.15) + 1.012)$$

203 where  $n_s$  is the nucleation site density ( $\text{m}^{-2}$ ) and  $T$  is the temperature (K). With  $n_s$  determined by  
204 MC2018, the nucleated ice particle concentration is obtained following Niemand et al. (2012) as

205 
$$\sum_{j=1}^n N_j = \sum_{j=1}^n N_{\text{tot},j} \{1 - \exp[-S_{\text{ae},j} n_s(T)]\}$$

206  
207 where  $S_{\text{ae},j}$  is the surface area of individual sea spray aerosol particles in the  $j^{\text{th}}$  bin which is  
208 calculated from  $\pi D_j^2/4$  ( $D_j$  is the geometric-mean diameter),  $N_{\text{tot},j}$  is the total sea spray aerosol  
209 number in each bin which is derived from its mass as detailed in the section above, and  $N_j$  is the  
210 ice particle number in each bin. Sea salt particles are used as the surrogate of sea spray aerosols  
211 given that most marine organic aerosols exist with coating on the surface of sea salt particles in  
212 the size range that dominates surface area (e.g., Prather et al., 2013). MC2018 can have efficient  
213 ice nucleation at warm temperatures like  $-15^\circ\text{C}$  or warmer.

214 Bigg et al. (1953) is employed only for homogeneous drop freezing when the temperature  
215 is colder than  $-37^\circ\text{C}$ . As discussed in Fan et al. (2014), the deposition-condensation freezing is  
216 turned off because the simulation with deposition-condensation freezing produces a large  
217 number of small ice particles, which is not consistent with the observed mixed-phase cloud  
218 properties in the study region. Contact freezing is also turned off due to the negligible  
219 contribution (Fan et al., 2014).

220

## 221 **2.2 Experiment design**

222 Simulations are configured with two nested domains using the nesting down approach  
223 (i.e., the inner domain is run separately driven by the outer domain), covering most of the



224 western US (Fig. 1). The outer domain consists of  $399 \times 399$  grid points with a horizontal grid  
225 spacing of 3 km and the inner domain consists of  $498 \times 390$  grid points with a horizontal grid  
226 spacing of 1 km. 50 vertical levels with stretched intervals are configured, with a grid spacing of  
227 70 m at the lowest levels and  $\sim 400$  m at the model top. The dynamics time step is 15 seconds for  
228 the outer domain and 5 seconds for the inner domain.

229 The simulation for the outer domain starts at 00:00 UTC on February 3 and runs for 48  
230 hours for chemistry spin-up using the WRF-Chem-SBM model, driven by global WRF-Chem  
231 simulation as the initial and boundary conditions of gas-phase species and aerosols and the  
232 Modern-Era Retrospective analysis for Research and Applications, Version 2 (MERRA2; spatial  
233 resolution of 0.5 by 0.5 degree and temporal resolution of 6-hourly) as the initial and boundary  
234 conditions of meteorological fields. Then the outer domain simulation is reinitialized at 00:00 UTC  
235 on February 5 using the meteorological data from MERRA2 to avoid the large error growth in  
236 meteorology associated with long-time model integration, although the chemistry simulations is a  
237 continuation from the spin-up run, and runs until 23:00 UTC on February 8. Given that running  
238 the WRF-Chem-SBM fully-coupled model is extremely computationally expensive for 1-km grid  
239 spacing in the inner domain, we interpolate aerosol-related quantities such as aerosol composition,  
240 hygroscopicity, and mass and number concentrations from the outer domain simulations using  
241 bilinear interpolation for the inner-domain simulation to reduce computational cost. This means  
242 we conduct the inner-domain simulation separately with chemistry turned off, and aerosol  
243 information is updated hourly using data from the outer domain simulations. The inner-domain  
244 simulation is run from 00:00 UTC on February 5 to 23:00 UTC on February 8, and the initial and  
245 boundary meteorological conditions are from MERRA2. To validate this approach, we compare  
246 the simulation with fully coupled WRF-Chem-SBM for the inner domain simulation and found



247 that the two simulations resemble each other in terms of precipitation (Fig. S1). Therefore, it is a  
248 valid approach that saves computation time by about 40%.

249 For emissions data, the U. S. Environment Protection Agency (EPA) National Emission  
250 Inventory (NEI) with a 4 km by 4 km horizontal resolution based on the year 2011 rates  
251 (NEI2011) is commonly used for anthropogenic emissions in the United States. However, using  
252 NEI2011 predicts too large anthropogenic aerosol mass compared with observations. Since the  
253 emissions of gaseous species and particulate matter decreased significantly from 2011 to 2015 in  
254 California (Table S1), the California Air Resources Board emission inventory in 2015  
255 (CARB2015) is used for anthropogenic emissions input for California, while NEI2011 is used  
256 for other states in the simulation domain. The use of NEI2011 for other states is acceptable since  
257 the lower and middle atmosphere in the simulation domain is dominated by southwesterly winds  
258 during the simulation period that transport air pollutants from coastal to inland regions. The use  
259 of CARB2015 reduces the simulation of aerosol number concentrations mainly below 2 km by  
260 40% relative to the use of NEI2011, in better agreement with observations.

261 The Model of Emissions of Gases and Aerosols from Nature (MEGAN) with a monthly  
262 temporal and 1 km horizontal resolution (Guenther et al., 2012) is used for biogenic emissions.  
263 The Rapid Radiative Transfer Model for application to GCMs (RRTMG) is used for shortwave  
264 and longwave radiation schemes (Iacono et al., 2008), the Noah Land Surface Model for land  
265 surface physics (Chen and Dudhia, 2001), and the Mellor-Yamada-Janjic (MYJ) scheme for  
266 planetary boundary layer parameterization (Mellor and Yamada, 1982; Janjić and Prediction,  
267 2001).

268 Three simulations were carried out over the inner domain for this study to investigate the  
269 impacts of marine INPs: (1) The reference case is Bigg, using the default immersion freezing



270 parameterization of Bigg et al. (1953) in SBM which is temperature-dependent only; (2)  
271 DM15+MC18, in which both DeMott et al. (2015) and MC2018 parameterizations are used for  
272 ice nucleation from dust and marine aerosols, respectively; (3) DM15, using the parameterization  
273 of DeMott et al. (2015) for dust aerosols (diameter  $> 0.5 \mu\text{m}$ ) with MC2018 turned off. The  
274 impacts of marine INPs are derived by comparing the DM15+MC18 and DM15 simulations.

## 275 **3 Results**

### 276 **3.1 Model evaluation with observations**

277 We evaluate the model simulations of aerosol and cloud properties and surface  
278 precipitation. Figure 2a shows a comparison of modeled aerosol properties including aerosol  
279 number concentration and chemical composition from the simulation of DM15+MC18 intended  
280 to represent the observed case, with the G-1 aircraft measurements on 7 February. Aerosol  
281 properties in all three simulations are similar, and thus only DM15+MC18 is shown. Overall, the  
282 simulated aerosol number concentration over the size range of  $0.067 - 3 \mu\text{m}$  is comparable to the  
283 observations over the same size range estimated by combining data from the Ultra-High-  
284 Sensitivity Aerosol Spectrometer (UHSAS) and the Passive Cavity Aerosol Spectrometer Probe  
285 (PCASP) at below 2-km altitude. The simulation overestimates the total aerosol number  
286 concentrations up to  $\sim 2$ -times at altitudes of 2.2-3.2 km. For aerosol composition, the airborne  
287 Aerosol Time of Flight Mass Spectrometry (ATOFMS) measurements provided the mean  
288 fractional number contributions of aerosol source classifications (Levin et al., 2019), which is  
289 shown in Fig. 2b. For comparison with the model, the mean mass contributions of the  
290 corresponding aerosol source classifications are computed since the number concentrations of  
291 individual aerosol components are not predicted by WRF-Chem (Fig. 2c). Both the observed  
292 fractional number contributions and the simulated mass contributions show that marine aerosols



293 are dominant during the AR event, accounting for more than 60% of the total aerosol number  
294 based on ATOFMS measurements and total aerosol mass based on the simulation. Although the  
295 simulated dust mass fraction is ~14%, the derived number concentration is very low (less than  
296  $0.02 \text{ cm}^{-3}$  for sizes larger than  $0.5 \mu\text{m}$ , shown in a later figure). This is because dust is mainly  
297 from aerosol bins at larger sizes. The number concentrations of the sea salt aerosols are generally  
298 three orders of magnitude higher than those of dust, and these numbers populate smaller bins of  
299 the aerosol distribution (97% from the first two aerosol size bins) even though the sea salt mass  
300 is predominately at larger sizes (96% from the last two size bins).

301 Figure 3 presents an evaluation of precipitation, showing the accumulated precipitation  
302 during the AR event from 06:00 UTC 5 February to 09:00 UTC 8 February 2015 (Fig. 3a) and  
303 the time-series of mean precipitation rates averaged over the observation stations (Fig. 3b). The  
304 observed precipitation rates are from the rain gauge measurements, provided by the NOAA Earth  
305 System Research Laboratory's Physical Sciences Division  
306 (<https://psl.noaa.gov/data/obs/datadisplay>). The model generally captures the spatial pattern of  
307 the observed accumulated precipitation (Fig. 3a) and reproduces the temporal evolution of the  
308 precipitation rate (Fig. 3b). Two major precipitation periods in the observations including the  
309 AR-induced orographic precipitation and the postfrontal precipitation are generally captured by  
310 the simulations, although the simulated postfrontal precipitation occurs several hours later in the  
311 simulations compared to the observations. The peak values of precipitation are overestimated by  
312 all the simulations (25-50%) relative to the observations (Fig. 3b), but the values from  
313 DM15+MC18 are lower than the other two, closer to the observations. From the spatial  
314 distributions (Fig. 3a), the observed accumulated precipitation in the southern part of the  
315 mountain range is generally less than 100 mm. DM15+MC18 simulates it well, whereas the



316 other two simulations overestimate precipitation in that area. The lower precipitation by  
317 DM15+MC18 is mainly because of the spillover effect caused by marine INPs (Fig. 3a, right).  
318 That is, with marine INPs, more ice/snow formed over the windward side falls slower than rain  
319 and more of them are transported to the lee side. In the northern part of the domain ( $> 40^\circ \text{N}$ ),  
320 DM15+MC18 predicts more precipitation than the other two simulations. The simulated  
321 precipitation between Bigg and DM15 are very similar, suggesting that in a low dust  
322 environment, the temperature-dependent Bigg (1953) parameterization simulates similar ice  
323 formation as DeMott et al. (2015).

324 Cloud phase is crucial to radiation and precipitation for mixed-phase clouds, and the  
325 glaciation ratio is usually used to represent the cloud phase states. The glaciation ratio is defined  
326 as  $(\text{IWC}/(\text{IWC}+\text{LWC}))$ , where LWC and IWC denote liquid and ice water content, respectively.  
327 Values less than 0.1 and larger than 0.9 denote the liquid phase and ice phase, respectively, with  
328 values between 0.1 and 0.9 for the mixed-phase (Korolev et al., 2003). The G-1 aircraft sampled  
329 the postfrontal clouds on February 7 as shown in Fig. 4a. All three simulations cannot capture the  
330 observed size of the precipitation cell (Figs. 4b and S2). In the simulations, precipitation is  
331 dominated by a few heavy precipitation clusters instead of the observed wide precipitation area.  
332 The simulated cells also do not reach the high altitudes found in the observations. The deviations  
333 of the simulation from observations for the postfrontal clouds could be mainly because of the  
334 long-time model integration time (the 4<sup>th</sup> day after model initiation). Anyhow, DM15+MC18  
335 simulates the largest size of the precipitation cell, with the highest vertical extent among the  
336 three simulations.

337 The LWC and IWC are derived from observations with the Water Content Monitor  
338 (WCM), an instrument that uses the impact of water on several heated wires as the basis for



339 measuring cloud total water content (TWC) and liquid water content (LWC) from which the ice  
340 water content (IWC) can be derived [Baumgardner et al., 2011; Matthews et al., 2015]. LWC and  
341 IWC along both horizontal and vertical flight segments are displayed in Fig. 5a-b. IWC is  
342 generally 2-4 times larger than LWC in the postfrontal clouds. To compare with observations,  
343 the model data are processed by: (a) selecting the grids at a distance from the simulated cell  
344 center similar to the distance of the airplane position from the observed postfrontal cell center,  
345 and sampling the data at a similar ambient temperature as observed by the aircraft (around  $-10\text{ }^{\circ}\text{C}$   
346 along the horizontal segment shown in Fig. 5a); (b) accounting for the location mismatch and  
347 increasing the sample size in the simulation to be more representative by extending the sampling  
348 area to include 20 grids at the front and back of a selected grid along the flight track, mimicking  
349 approximately the distance traveled by the G-1 airplane in five minutes; (c) filtering out the  
350 sampled grids with values of (LWC + IWC) below the detection limit of WCM (i.e.,  $0.02\text{ g m}^{-3}$ ,  
351 Thompson et al., 2016). Both horizontal and vertical flight segments are incorporated for  
352 comparison.

353 Figure 5 shows comparisons of LWC and IWC and the glaciation ratio of  
354  $\text{IWC}/(\text{IWC}+\text{LWC})$  between the simulations and aircraft measurements. LWC is overestimated in  
355 all three simulations, while IWC is underestimated in Bigg and DM15 but overestimated in  
356 DM15+MC18 (Fig. 5c). The mean glaciation ratios fall in the range of 0.1- 0.9 among the  
357 simulations (Fig. 5d), indicating that the observed mixed-phase cloud feature is simulated by the  
358 model. DM15+MC18 shows a mean ratio of  $\sim 0.70$ , similar to the observed value of 0.74. This  
359 shows that the mixed-phase state is well captured when the marine INP effect is considered. In  
360 contrast, in Bigg and DM15 with a glaciation ratio is 0.41 or less, the mixed-phase state is liquid-  
361 dominated. The inclusion of the marine INP effect improves the simulation of cloud phase states





362 via enhancing heterogenous ice formation through immersion freezing. A detailed examination  
363 of how the marine INPs impacts ice nucleation and cloud properties will be discussed in the  
364 following section.

365

### 366 **3.2 Marine INP effects under different AR stages**

367 Impacts of the marine INPs transported from the Pacific Ocean on orographic clouds and  
368 precipitation are revealed by comparing the simulation of DM15+MC18 with the simulation of  
369 DM15.

370 The AR evolution has three distinct stages: before AR landfall (from 06:00 UTC 5 to  
371 18:00 UTC 6 February), after AR landfall (from 18:00 UTC 6 to 12:00 UTC 7 February), and  
372 post-AR (from 12:00 UTC 7 to 09:00 UTC 8 February). The three stages can be identified from  
373 the change of the integrated water vapor (IWV) with time during the event (Fig. 6a). Before AR  
374 landfall, IWV in most of California was relatively low (Fig. 6a, left). IWV in northern California  
375 increased as the AR made landfall at about 18:00 UTC on 6 February and brought ample water  
376 vapor to California (Fig. 6a, middle). Heavy orographic precipitation along the Sierra Nevada  
377 Mountains occurred during this period (Fig. 7a). At 12:00 UTC 7 February, the AR started to  
378 retreat (Fig. 6a, right), and postfrontal cloud cells formed, with relatively small cloud fraction  
379 and precipitation (Fig. 7a).

380 Vertical profiles of the thermodynamic and kinematic environments at the three stages  
381 are shown in Fig. 6b. The thermodynamic and kinematic environments significantly varied with  
382 the AR stages. After AR landfall, water vapor increased significantly in the lower atmosphere  
383 (below 5 km), but the middle and upper levels became drier (dashed, Fig. 6b) compared with the  
384 stage before AR landfall (solid). The vertical motion also weakened after AR landfall (Fig. 6d),



385 suggesting that the atmosphere became more stable. At the post-AR stage, moisture above 2-km  
386 altitude was reduced compared to after AR landfall. Note that the temperature below 8 km was  
387 colder by up to 6 °C at the post-AR stage compared to the previous two stages (Fig. 6c). These  
388 differences in the meteorological conditions among the different stages are very important to  
389 understand the cloud and precipitation properties and their responses to marine INPs. The mean  
390 water vapor and temperature profiles are similar between DM15 (blue) and DM15+MC18 (red),  
391 as seen from the overlapping blue and red lines.

392 From the time series of average precipitation rates (Fig. 7a), the effect of marine INPs  
393 varies with the different AR stages, from substantial increases of precipitation (up to 330%)  
394 before AR landfall (the red dotted line, second y-axis) to no significant effects (a very small  
395 increase) after AR landfall. In the first stage (before AR landfall), the total precipitation increases  
396 by 36% on average due to the marine INP effect (Fig. 7a and Table 1). There is only a 4%  
397 increase in the total precipitation after AR landfall. The total precipitation at the post-AR stage is  
398 small and the change from DM15 and DM15+MC18 is negligible. Thus, the marine INP effect  
399 only significantly increases the total precipitation over the domain at the stage before AR landfall  
400 when a moderate amount of precipitation occurs in northern California (Fig. 8a). After AR  
401 landfall, precipitation increases significantly. Although the total precipitation is not changed  
402 much by the marine INPs, the marine INPs produce a spillover effect featuring reduced  
403 precipitation on the windward slope of the mountains but increased precipitation over the lee side  
404 (Fig. 8b and Fig. 9e). This is because with the marine INPs, the larger amount of ice/snow that  
405 forms on the windward slope is transported to the lee side (Fig. 9d) and grows to a larger size  
406 and precipitates as snow. This spillover effect is accompanied by a large reduction of cloud water  
407 and rain over the windward side because of conversion of liquid to ice (Fig. 9b-c). Since the



408 water vapor transport along the cross-section is very similar between DM15 and DM15+MC18  
409 (Fig. 9a), the spillover effect by marine INPs is mainly the result of different cloud  
410 microphysical properties instead of meteorological conditions.

411 Even though the total domain precipitation is not changed much by the marine INPs at  
412 the later two stages, the cloud phase and the near-surface precipitation type (i.e., rain or snow)  
413 are notably changed (Table 1). The mean glaciation ratio in the mixed-phase is very low in  
414 DM15 (0.14, 0.16, and 0.001 for the 1<sup>st</sup>, 2<sup>nd</sup>, and 3<sup>rd</sup> stages, respectively) and is increased to 0.74,  
415 0.59, and 0.36, respectively. We examine the ratio of snow/(rain+snow) in mass mixing ratio at  
416 the lowest model level for the changes of the near-surface precipitation type (Fig. 7b). There is  
417 negligible snow precipitation near the surface in DM15 and the ratios of snow precipitation are  
418 very small during the entire AR event. The snow precipitation ratios increase in DM15+MC18  
419 and the magnitudes vary significantly with different AR stages. On average, the ratio of snow  
420 precipitation increases from 0.002, 0.001, <0.001 in DM15 to 0.08, 0.04, and 0.13 in  
421 DM15+MC18 before AR landfall, after AR landfall, and post-AR, respectively (Table 1). This  
422 shows that the marine INPs increase snow precipitation and the effect is particularly significant  
423 before AR landfall and post-AR. Correspondingly, rain precipitation is reduced (Table 1). This  
424 has an important implication for the regional hydrological resource since more snow  
425 accumulation in winter increases freshwater resources in the summer while less rain reduces  
426 flood risks.

427 The increased snow and reduced rain at the surface correspond to the increased ice water  
428 path (IWP) and decreased liquid water path (LWP; Fig. 7c). The mean LWP in DM15+MC18 is  
429 reduced by 66%, 46%, and 26% for the three stages relative to DM15, respectively (Table 1). We  
430 showed an increased LWC from DM15 to DM15+MC18 in Figure 5c in the postfrontal cells.



431 Here the decrease in LWC/LWP averaged over the entire post-AR stage is dominated by the  
432 strong decrease over the time before the postfrontal cloud formed. The postfrontal cells are  
433 invigorated (see section 3.3) by marine INPs so both LWC and IWC are increased as shown in  
434 Figure 5. IWP is greatly enhanced by about 8, 5, and 440 times at the three stages, respectively.  
435 Interestingly, the total condensate water path (TWP) is increased by the marine INPs (Fig. 7d).  
436 On average there are 45%, 29%, and 35% increases in TWP in DM15+MC18 at the three AR  
437 stages relative to DM15, respectively (Table 1). The increases in the total condensate water path  
438 and the increased surface precipitation (or no change) suggest that marine INPs enhance the  
439 conversion of water from the vapor phase to the condensate phase, which will be further  
440 discussed later. This is particularly the case before AR landfall with water vapor content notably  
441 reduced in DM15+MC18 compared with DM15 (Fig. S3a).

442 Cloud cover is slightly increased during the first two stages (4-5%) in the simulations  
443 including marine INPs, but the change at the post-AR stage is  $\sim 20\%$  on average, which is very  
444 significant. Because both TWP and cloud cover are increased due to the marine INP effect, the  
445 cloud radiative forcing (CRF) at TOA gets stronger by 15%, 13%, and 10% for the three AR  
446 stages, respectively. Although the cloud phase, precipitation type, and cloud fraction at the post-  
447 AR stage have the largest changes among the three stages by the marine INP effect (Table 1), the  
448 CRF does not change drastically probably because of the offset between the increase resulting  
449 from the increased cloud fraction and TWP and the decrease from the reduced cloud liquid is the  
450 largest.

451 Overall, the marine INP effects on TWP, IWP, and snow precipitation are more  
452 significant at the first and third stages (i.e., before AR landfall and post-AR) than the stage after  
453 AR landfall. But a notable spillover effect is seen after AR landfall. The cloud and precipitation



454 quantities are more sensitive to marine INPs before AR landfall than after AR landfall, and the  
455 responses of TWP/IWP and snow precipitation are particularly drastic at the post-AR stage  
456 (Table 1). The reasons leading to the different responses at different AR stages are now  
457 examined.

458

### 459 **3.3 Explaining different marine INP effects at different AR stages**

460 We first examine the temporal evolution of dust and marine aerosol number  
461 concentrations, which are derived based on the predicted mass mixing ratios as described in  
462 Section 2 and used as input to the DeMott et al. (2015) and MC2018 parameterizations (Fig. 10a,  
463 b), as well as their corresponding immersion freezing (i.e., ice nucleation) rates (Fig. 10c, d). The  
464 dust concentrations and the corresponding ice nucleation rates (Fig. 10a, c) are about three orders  
465 of magnitude lower than those of the marine aerosols (Fig. 10b, d) during the AR events. This is  
466 driven both by the activation temperature spectrum of dust and its very low mass/number  
467 concentrations in this case. Ice nucleation from dust is negligible at temperatures warmer than -  
468 15 °C but the ice nucleation from marine aerosols is notable. This is mainly because of three  
469 orders of magnitude higher marine aerosol number concentrations from the surface up to 8 km.  
470 The deep marine aerosol layer during the AR allows notable ice nucleation at temperatures  
471 higher than -15 °C. The clear-sky marine aerosol number concentrations increase from before  
472 AR landfall to post-AR as the AR evolved (Fig. 10b). After the AR makes landfall, marine  
473 aerosols increase significantly as AR strong winds near the ocean surface produce them more  
474 and also transport more to the Sierra Nevada Mountains (Fig. 10b). Despite the significant  
475 increase in marine aerosols after AR landfall, the marine INP effects on clouds and precipitation  
476 are small at this stage, because the increase of marine aerosols does not increase ice nucleation



477 rates (Fig. 10d). However, at the post-AR stage, the ice nucleation rates from the marine INPs  
478 are up to a few times larger than the earlier two stages (Fig. 10d), explaining why the effects on  
479 IWP and snow precipitation at the post-AR stage are largest among the three stages.

480 To further understand how and why the cloud and precipitation responses to marine INPs  
481 are different at different AR stages, we separate clouds into three cloud regimes: a shallow warm  
482 cloud regime with cloud top temperature (CTT) warmer than 0 °C, a mixed-phase cloud regime  
483 with CTT between -30 and 0 °C, and a deep cloud regime having CTT colder than -30 °C and  
484 cloud base temperatures above 0 °C. Figure 11 shows that the marine INP effect consistently  
485 shifts the cloud occurrences from the shallow warm cloud regime to mixed-phase and/or deep  
486 cloud regimes among the three AR stages. It is noted that the deep cloud regime is enhanced  
487 much more at the first and third stages than the second stage, i.e., 22% before AR landfall and  
488 235% at the post-AR stage but only 8% after AR landfall. The post-AR stage also has the largest  
489 increase in mixed-phase cloud occurrences.

490 Accordingly, the mean cloud depth for each cloud regime is changed by marine INPs,  
491 with a decrease for the shallow warm clouds and an increase for the mixed-phase and deep  
492 clouds (Fig. 11b). Before AR landfall, the increase in the deep cloud depth is largest while at the  
493 post-AR stage, the increase in the mixed-phase cloud depth is the largest. Consistent with a shift  
494 in cloud regimes, the total precipitation produced by shallow warm clouds is reduced by 9%,  
495 22%, and 16% while the total precipitation produced by deep clouds is increased by 66%, 4%,  
496 and 350%, respectively, at the three AR stages (Fig. 11c). Therefore, the large increase in the  
497 surface accumulated precipitation by marine INPs before AR landfall (36%) is mainly because of  
498 the increase in deep cloud precipitation. The larger occurrence of deep clouds at this stage is  
499 consistent with a larger increase in TWP and reduction in moisture. Although the relative



500 increases in deep cloud occurrences and precipitation by marine INPs are very large at the post-  
501 AR stage, their occurrences are so small that their contribution to the total precipitation is  
502 negligible.

503           How do marine INPs reduce shallow warm clouds but invigorate mixed-phase and deep  
504 clouds and why is this effect larger at the first and third stages? Marine INPs greatly enhance ice  
505 and snow number concentrations and mass mixing ratios through immersion freezing, which  
506 converts drops to ice or snow particles (Figs. 12a and 13a). The mean number concentrations  
507 and mass mixing ratios of ice particles (ice +snow) in mixed-phase and deep cloud regimes are  
508 several orders of magnitude higher in DM15+MC18 than in DM15. As detailed in Fan et al.  
509 (2017a) which studied the same type of mixed-phase clouds in the same region, more ice/snow  
510 particles forming from the immersion freezing enhance the Wegener–Bergeron–Findeisen  
511 (WBF) and riming processes (Table 2), converting supercooled drops to ice or snow and leading  
512 to more ice/snow but fewer cloud droplets and raindrops (Figs. 12b, c and 13b, c). The  
513 reductions of cloud droplet and raindrop number concentrations and mass mixing ratios from  
514 DM15 to DM15+MC18 are larger before AR landfall and during post-AR relative to the stage  
515 after AR landfall, corresponding to a larger shift to the mixed-phase and deep clouds. Thus, the  
516 larger increases in deposition/WBF and riming rates are seen (Table 2).

517           As discussed earlier, the largest ice nucleation rates at the post-AR stage explain the  
518 largest marine INP effects among the three stages. The postfrontal clouds have the lower cloud  
519 top heights (warmer than  $-25$  °C, i.e., shallower clouds) compared with the clouds at the first two  
520 stages, thus the dust INP nucleation rates are smaller (negligible) as shown in Fig. 10c but the  
521 deep marine aerosol layer and its action as INPs adds significantly to ice nucleation. In addition,  
522 with the  $\sim 6$  °C colder temperatures below 8-km altitudes during the post-AR stage compared to



523 the other two stages, ice nucleation from marine aerosols becomes more efficient (Fig. 10d). The  
524 mostly significantly invigorated postfrontal cloud cells by the marine INP effect (i.e., the  
525 increase in both LWC and IWC and a large increase in cloud fraction) might also be related to  
526 small scale thermodynamic changes through the feedback of microphysical changes over the first  
527 two AR stages.

528 As for why increases of deep cloud occurrence and precipitation are less significant after  
529 AR landfall compared to before AR landfall, first, we see the ice nucleation rates from dust INPs  
530 is larger after AR landfall (the largest among the three stages; Fig. 10c), because of the increased  
531 dust loading due to stronger transport (Fig. 10a). Stronger dust INP effects would limit the  
532 marine INP effects since they compete for liquid drops. Second, the moisture increase after AR  
533 landfall occurs in the lower atmosphere while the middle- and upper-level atmosphere are much  
534 drier than before AR landfall (Fig. 6d), which favors more warm clouds and rain but is less  
535 favorable to ice cloud development as indicated by the smallest ratio of snow precipitation (Fig.  
536 7b). For more warm clouds/rain-dominated situations, the enhancement of ice formation would  
537 have less influence. Furthermore, in the drier condition aloft, more ice formation means less  
538 efficient growth, thus the impacts on IWC/IWP and precipitation would be smaller. Cloud  
539 dynamics (vertical velocity) is not changed much by the marine INP effect at all three stages,  
540 indicating that the feedback from the increased latent heating resulting from enhanced deposition  
541 and riming does not play an important role here, likely because this is not a convective  
542 environment.

#### 543 **4 Conclusion and discussion**

544 We have explored the effects of INPs from sea spray aerosols transported from the  
545 Pacific Ocean on wintertime mixed-phase stratiform cloud properties and precipitation





546 associated with atmospheric river (AR) events. This is done by carrying out simulations at a  
547 cloud-resolving scale (1 km) using WRF-Chem coupled with the spectral-bin microphysics  
548 (SBM) scheme for an AR event observed during the 2015 Atmospheric Radiation Measurement  
549 Cloud Aerosol Precipitation Experiment (ACAPEX). We have implemented the ice nucleation  
550 parameterization for marine aerosols (McCluskey et al. 2018a) into SBM to account for the  
551 marine INP effect. By comparing with available airborne and ground-based observations, we  
552 show that considering the marine INP effect in the model improves the simulation of cloud phase  
553 states (i.e., increased glaciation ratio) and precipitation.

554 Through enhancing ice and snow formation, marine INPs greatly enhance WBF and  
555 riming processes, which convert liquid clouds to mixed-phase and ice clouds. There is a notable  
556 shift in cloud occurrences with reduced shallow warm clouds (44%, 26%, and 7% for before and  
557 after AR landfall and the post-AR stages, respectively) and increased mixed-phase (10%, 7%,  
558 and 38% ) and/or deep cloud regimes (~ 22%, 8%, and 230%) because of the marine INP effect.  
559 As a result, large increases in the ice water path (5 times or more), total condensate water path  
560 (29% or more), and the ratio of snow precipitation (40 times or more) are seen. There is an  
561 enhanced conversion of water from the vapor phase to the condensate phase so the water vapor is  
562 generally reduced with the marine INP effect considered.

563 The significance of the above-described marine INP effects varies with the AR stages,  
564 with a larger effect before AR landfall and post-AR than after AR landfall that has the dominant  
565 precipitation. Note that the marine INP effects on cloud properties and snow precipitation are  
566 still notable even at the stage after AR landfall. Although the total precipitation increases only by  
567 4%, the drastic increase of snow precipitation and reduced rain precipitation at the surface have  
568 an important implication for the regional water resources and flood risks since more snow



569 increases freshwater resources while less rain reduces flash flood risks. In addition, at this stage,  
570 the marine INPs produce a notable spillover effect with a precipitation decrease (up to 30%) over  
571 the windward slope of the mountains but precipitation (snow) over the lee side is doubled,  
572 because more ice/snow formed over the windward side falls slower than rain and more easily  
573 transported to the lee side.

574 Several reasons can be responsible for the smaller marine INP effects on cloud properties  
575 (particularly reduction of shallow warm clouds and increased mixed-phase and deep clouds) and  
576 snow precipitation after AR landfall compared with before AR landfall. First, the dust INP  
577 effects are larger at this stage, which would limit the marine INP effect since they compete for  
578 liquid drops. Second, after AR landfall, the moisture is heavily concentrated at the lower  
579 atmosphere while the middle- and upper-level atmosphere are much drier than before AR  
580 landfall. Therefore, the environment is more warm cloud and rain dominated, limiting the effects  
581 of enhanced ice formation. Furthermore, in the drier condition, more ice formation means less  
582 efficient growth, thus the impacts on IWC/IWP and precipitation would be smaller.

583 The post AR stage has the largest response of the cloud regime shift and snow  
584 precipitation among the three stages, because of the largest ice nucleation rates from the marine  
585 aerosols. The larger ice nucleation rates compared with the other two stages are probably  
586 because the lower cloud top heights (warmer than  $-25^{\circ}\text{C}$ , i.e., shallower clouds) limit dust INP  
587 nucleation, and with  $\sim 6^{\circ}\text{C}$  colder temperatures below 8-km altitudes than the other two stages,  
588 ice nucleation from the deep marine aerosol layer is more efficient.

589 This study suggests that the inclusion of marine INPs enhances orographic precipitation  
590 mainly through more efficient growth (deposition and riming) of a larger number of ice particles  
591 than liquid droplets, which is consistent with literature studies (Mühlbauer and Lohmann, 2009;



592 Fan et al., 2014, 2017; Xiao et al., 2015). The spillover effect by the increase of CCN has been  
593 presented in several previous studies (e.g., Mühlbauer and Lohmann, 2008, 2009; Saleeby et al.,  
594 2011, 2013; Carrio and Cotton, 2014; Letcher and Cotton, 2014). To our knowledge, this study is  
595 the first to show the spillover effect associated with the INP effect. The prominent spillover  
596 effect by the marine INP is different from Fan et al. (2014, 2017) that did not find such an effect  
597 by dust INPs. There are a couple of factors that might be responsible for the difference. First,  
598 marine INPs are mainly brought by ARs so the windward side gets INP first while dust INPs are  
599 not associated with AR so there is no temporal sequence to have dust between the windward and  
600 Lee sides. Second, the AR event is different with a different wind direction and speed, which  
601 makes the transport of ice/snow to the lee side easier.

602 The marine INP effect revealed in this study is clearly emphasized due to the very low  
603 dust INP concentrations for this particular situation and the deep marine aerosol layer during the  
604 AR which allows notable ice nucleation at temperatures higher than  $-15\text{ }^{\circ}\text{C}$ . With high dust INPs,  
605 the effects of marine INPs might not be as significant since they compete for supercooled liquid  
606 drops. Although this is a single case study, the AR event and its evolution are representative.  
607 Thus, the study suggests the importance of accounting for marine aerosols as INPs, in addition to  
608 long-range transported mineral dusts, to simulate winter clouds and precipitation in the western  
609 United States in regional and global climate models. We employ an empirical parameterization  
610 for marine INPs developed from the data collected over the northern Atlantic Ocean and use sea  
611 salt aerosols as a surrogate of marine organics, which might produce some uncertainties.  
612 Nevertheless, the marine INP parameterization appears representative for this region based on  
613 Levin et al. (2019). More observational data are needed in the western U.S. for (a) developing ice  
614 nucleation parameterizations for potentially variable marine organics and (b) understanding



615 marine organics emission and chemical mechanisms and accurately simulating marine organics  
616 in the model. As discussed earlier, the conversion of mass to number concentrations over each  
617 aerosol bin might introduce some uncertainty to this study, which calls for model developments  
618 of predicting the number concentration of each aerosol component.

619

620 **Data availability.**

621 The observational data can be accessed from the ARM data archive,  
622 <https://www.arm.gov/research/campaigns/amf2015apex>. The model simulation data will be  
623 available through the NERSC data repository after the paper is accepted.

624

625 **Supplement.**

626 The supplement related to this article is available online.

627

628 **Author contributions.**

629 JF designed the study and model experiments. YL, JF, and PL performed numerical simulations  
630 and analyses. JF and YL wrote the paper and other authors commented on it. LRL, PJD, LG, JF,  
631 JT, YL, and JHJ contributed by either processing data including model input and observational  
632 data or participating in the discussion of results.

633

634 **Competing interests.**

635 The authors declare that they have no conflict of interest.



636 **Acknowledgments.**

637 This research used resources of the PNNL Institutional Computing (PIC), and National Energy  
638 Research Scientific Computing Center (NERSC). NERSC is a U.S. DOE Office of Science User  
639 Facility operated under Contract No. DE-AC02-05CH11231. Funding for ACAPEX that  
640 provides data collected on the G-1 aircraft was supported by the Atmospheric Radiation  
641 Measurement (ARM) user facility, a U.S. Department of Energy (DOE) Office of Science user  
642 facility managed by the Office of Biological and Environmental Research. The deployment of  
643 the G-1 also involved the assistance of many PNNL/ARM field staff including M. Hubbell and  
644 C. Eveland who flew the G-1 during ACAPEX. The authors acknowledge California Air  
645 Resources Board for providing the 2015 emission inventory data and Dr. Allen White from  
646 NOAA's Physical Sciences Laboratory for providing rainfall gauge data, and thank Alyssa  
647 Matthews and Jingyu Wang at PNNL and Yuan Wang at JPL for technical/data discussion.  
648

649 **Financial support.**

650 This study was supported by the Office of Science of U.S. Department of Energy Biological and  
651 Environmental Research through the Regional and Global Model Analysis program area that  
652 supports the Water Cycle and Climate Extremes Modeling (WACCEM) Science Focus Area at  
653 PNNL and the DOE Early Career Research Program (project # 70071). PNNL is operated for the  
654 U.S. Department of Energy (DOE) by Battelle Memorial Institute under contract DE-AC05-  
655 76RL01830.



## 656 Reference

- 657 Ault, A. P., Williams, C. R., White, A. B., Neiman, P. J., Creamean, J. M., Gaston, C. J., Ralph,  
658 F. M., and Prather, K. A.: Detection of Asian dust in California orographic precipitation,  
659 116, 1–15, <https://doi.org/10.1029/2010JD015351>, 2011.
- 660 Baumgardner, D., et al. (2011), Airborne instruments to measure atmospheric aerosol particles,  
661 clouds and radiation: A cook's tour of mature and emerging technology, *Atmos. Res.*,  
662 102(1), 10–29
- 663 Bigg, E. K.: The Formation of Atmospheric Ice Crystals by the Freezing of Droplets, 79, 510–  
664 519, <https://doi.org/10.1002/qj.49707934207>, 1953.
- 665 Burrows, S. M., Hoose, C., Pöschl, U., and Lawrence, M. G.: Ice nuclei in marine air: Biogenic  
666 particles or dust?, 13, 245–267, <https://doi.org/10.5194/acp-13-245-2013>, 2013.
- 667 Carrió, G.G., Cotton, W.R., 2014. On the buffering of CCN impacts on wintertime orographic  
668 clouds: an idealized examination, *Atmos. Res.* 137, 136–144.
- 669 Chen, F. and Dudhia, J.: Coupling an Advanced Land Surface–Hydrology Model with the Penn  
670 State–NCAR MM5 Modeling System. Part I: Model Implementation and Sensitivity, 129,  
671 569–585, [https://doi.org/https://doi.org/10.1175/1520-  
672 0493\(2001\)129<0569:Caalsh>2.0.Co;2](https://doi.org/https://doi.org/10.1175/1520-0493(2001)129<0569:Caalsh>2.0.Co;2), 2001.
- 673 Choulaton, T. W. and Perry, S. J.: A model of the orographic enhancement of snowfall by the  
674 seeder-feeder mechanism, 112, 335–345,  
675 <https://doi.org/https://doi.org/10.1002/qj.49711247204>, 1986.
- 676 Choudhury, G., B. Tyagi, J. Singh, C. Sarangi, S.N. Tripathi. Aerosol-orography-precipitation –  
677 a critical assessment, *Atmos. Environ.*, 214 (116831) (2019), pp. 1-19,  
678 [10.1016/j.atmosenv.2019.116831](https://doi.org/10.1016/j.atmosenv.2019.116831).
- 679 Cordeira, J. M., Ralph, F. M., Martin, A., Gaggini, N., Spackman, J. R., Neiman, P. J., Rutz, J. J.,  
680 and Pierce, R.: Forecasting atmospheric rivers during calwater 2015, 98, 449–459,  
681 <https://doi.org/10.1175/BAMS-D-15-00245.1>, 2017.
- 682 Creamean, J. M., Suski, K. J., Rosenfeld, D., Cazorla, A., DeMott, P. J., Sullivan, R. C., White,  
683 A. B., Ralph, F. M., Minnis, P., Comstock, J. M., Tomlinson, J. M., and Prather, K. A.: Dust  
684 and Biological Aerosols from the Sahara and Asia Influence Precipitation in the Western  
685 U.S, 339, 1572–1578, <https://doi.org/10.1126/science.1227279>, 2013.
- 686 Creamean, J. M., Ault, A. P., White, A. B., Neiman, P. J., Ralph, F. M., Minnis, P., and Prather,  
687 K. A.: Impact of interannual variations in sources of insoluble aerosol species on orographic  
688 precipitation over California's central Sierra Nevada, 15, 6535–6548,  
689 <https://doi.org/10.5194/acp-15-6535-2015>, 2015.
- 690 DeMott, P. J., Prenni, A. J., Liu, X., Kreidenweis, S. M., Petters, M. D., Twohy, C. H.,  
691 Richardson, M. S., Eidhammer, T., and Rogers, D. C.: Predicting global atmospheric ice  
692 nuclei distributions and their impacts on climate, 107, 11217–11222,  
693 <https://doi.org/10.1073/pnas.0910818107>, 2010.
- 694 DeMott, P. J., Prenni, A. J., McMeeking, G. R., Sullivan, R. C., Petters, M. D., Tobo, Y.,  
695 Niemand, M., Möhler, O., Snider, J. R., Wang, Z., and Kreidenweis, S. M.: Integrating  
696 laboratory and field data to quantify the immersion freezing ice nucleation activity of  
697 mineral dust particles, 15, 393–409, <https://doi.org/10.5194/acp-15-393-2015>, 2015.
- 698 DeMott, P. J., Hill, T. C. J., McCluskey, C. S., Prather, K. A., Collins, D. B., Sullivan, R. C.,  
699 Ruppel, M. J., Mason, R. H., Irish, V. E., Lee, T., Hwang, C. Y., Rhee, T. S., Snider, J. R.,  
700 McMeeking, G. R., Dhaniyala, S., Lewis, E. R., Wentzell, J. J. B., Abbatt, J., Lee, C.,



- 701 Sultana, C. M., Ault, A. P., Axson, J. L., Martinez, M. D., Venero, I., Santos-Figueroa, G.,  
702 Stokes, M. D., Deane, G. B., Mayol-Bracero, O. L., Grassian, V. H., Bertram, T. H.,  
703 Bertram, A. K., Moffett, B. F., and Franc, G. D.: Sea spray aerosol as a unique source of ice  
704 nucleating particles, 113, 5797–5803, <https://doi.org/10.1073/pnas.1514034112>, 2016.
- 705 Dettinger, M. D., Ralph, F. M., Das, T., Neiman, P. J., and Cayan, D. R.: Atmospheric Rivers,  
706 Floods and the Water Resources of California, <https://doi.org/10.3390/w3020445>, 2011.
- 707 Fan, J., Leung, L. R., Li, Z., Morrison, H., Chen, H., Zhou, Y., Qian, Y., and Wang, Y.: Aerosol  
708 impacts on clouds and precipitation in eastern China: Results from bin and bulk  
709 microphysics, 117, <https://doi.org/https://doi.org/10.1029/2011jd016537>, 2012.
- 710 Fan, J., Leung, L. R., DeMott, P. J., Comstock, J. M., Singh, B., Rosenfeld, D., Tomlinson, J.  
711 M., White, A., Prather, K. A., Minnis, P., Ayers, J. K., and Min, Q.: Aerosol impacts on  
712 California winter clouds and precipitation during CalWater 2011: local pollution versus  
713 long-range transported dust, 14, 81–101, <https://doi.org/10.5194/acp-14-81-2014>, 2014.
- 714 Fan, J., Han, B., Varble, A., Morrison, H., North, K., Kollias, P., Chen, B., Dong, X.,  
715 Giangrande, S. E., Khain, A., Lin, Y., Mansell, E., Milbrandt, J. A., Stenz, R., Thompson,  
716 G., and Wang, Y.: Cloud-resolving model intercomparison of an MC3E squall line case:  
717 Part I—Convective updrafts, 122, 9351–9378, <https://doi.org/10.1002/2017JD026622>,  
718 2017a.
- 719 Fan, J., Leung, L. R., Rosenfeld, D., and DeMott, P. J.: Effects of cloud condensation nuclei and  
720 ice nucleating particles on precipitation processes and supercooled liquid in mixed-phase  
721 orographic clouds, 17, 1017–1035, <https://doi.org/10.5194/acp-17-1017-2017>, 2017b.
- 722 Fast, J. D., Gustafson Jr., W. I., Easter, R. C., Zaveri, R. A., Barnard, J. C., Chapman, E. G.,  
723 Grell, G. A., and Peckham, S. E.: Evolution of ozone, particulates, and aerosol direct  
724 radiative forcing in the vicinity of Houston using a fully coupled meteorology-chemistry-  
725 aerosol model, 111, <https://doi.org/https://doi.org/10.1029/2005jd006721>, 2006.
- 726 French, J. R., Friedrich, K., Tessendorf, S. A., Rauber, R. M., Geerts, B., Rasmussen, R. M.,  
727 Xue, L., Kunkel, M. L., and Blestrud, D. R.: Precipitation formation from orographic cloud  
728 seeding, 115, 1168 LP – 1173, <https://doi.org/10.1073/pnas.1716995115>, 2018.
- 729 Gao, W., Fan, J., Easter, R. C., Yang, Q., Zhao, C., and Ghan, S. J.: Coupling spectral-bin cloud  
730 microphysics with the MOSAIC aerosol model in WRF-Chem: Methodology and results for  
731 marine stratocumulus clouds, 8, 1289–1309,  
732 <https://doi.org/10.1002/2016MS000676>.Received, 2016.
- 733 Geerts, B., Miao, Q., Yang, Y., Rasmussen, R., and Breed, D.: An Airborne Profiling Radar  
734 Study of the Impact of Glaciogenic Cloud Seeding on Snowfall from Winter Orographic  
735 Clouds, 67, 3286–3302, <https://doi.org/10.1175/2010JAS3496.1>, 2010.
- 736 Gong, S. L., Barrie, L. A., and Blanchet, J. P.: Modeling sea-salt aerosols in the atmosphere 1.  
737 Model development, 102, 3805–3818, <https://doi.org/10.1029/96jd02953>, 1997a.
- 738 Gong, S. L., Barrie, L. A., Prospero, J. M., Savoie, D. L., Ayers, G. P., Blanchet, J. P., and  
739 Spacek, L.: Modeling sea-salt aerosols in the atmosphere 2. Atmospheric concentrations and  
740 fluxes, 102, 3819–3830, <https://doi.org/10.1029/96jd03401>, 1997b.
- 741 Guenther, A. B., Jiang, X., Heald, C. L., Sakulyanontvittaya, T., Duhl, T., Emmons, L. K., and  
742 Wang, X.: The Model of Emissions of Gases and Aerosols from Nature version 2.1  
743 (MEGAN2.1): an extended and updated framework for modeling biogenic emissions, 5,  
744 1471–1492, <https://doi.org/https://doi.org/10.5194/gmd-5-1471-2012>, 2012.



- 745 Hazra, A., Padmakumari, B., Maheskumar, R. S., and Chen, J. P.: The effect of mineral dust and  
746 soot aerosols on ice microphysics near the foothills of the Himalayas: A numerical  
747 investigation, 171, 41–55, <https://doi.org/10.1016/j.atmosres.2015.12.005>, 2016.
- 748 Hoose, C., Kristjánsson, J. E., and Burrows, S. M.: How important is biological ice nucleation in  
749 clouds on a global scale?, 5, 24009, <https://doi.org/10.1088/1748-9326/5/2/024009>, 2010.
- 750 Iacono, M. J., Delamere, J. S., Mlawer, E. J., Shephard, M. W., Clough, S. A., and Collins, W.  
751 D.: Radiative forcing by long-lived greenhouse gases: Calculations with the AER radiative  
752 transfer models, 113, <https://doi.org/https://doi.org/10.1029/2008jd009944>, 2008.
- 753 Janjić, Z. I. and Prediction, N. C. for E.: Nonsingular implementation of the Mellor-Yamada  
754 level 2.5 scheme in the NCEP Meso model, 2001.
- 755 Kanji, Z. A., Ladino, L. A., Wex, H., Boose, Y., Burkert-Kohn, M., Cziczo, D. J., and Krämer,  
756 M.: Overview of Ice Nucleating Particles, 58, 1.1-1.33,  
757 <https://doi.org/10.1175/amsmonographs-d-16-0006.1>, 2017.
- 758 Khain, A., Lynn, B., and Dudhia, J.: Aerosol Effects on Intensity of Landfalling Hurricanes as  
759 Seen from Simulations with the WRF Model with Spectral Bin Microphysics, 67, 365–384,  
760 <https://doi.org/doi:10.1175/2009JAS3210.1>, 2010.
- 761 Khain, A. P., Leung, L. R., Lynn, B., and Ghan, S.: Effects of aerosols on the dynamics and  
762 microphysics of squall lines simulated by spectral bin and bulk parameterization schemes,  
763 114, <https://doi.org/10.1029/2009jd011902>, 2009.
- 764 Korolev, A. v, Isaac, G. A., Cober, S. G., Strapp, J. W., and Hallett, J.: Microphysical  
765 characterization of mixed-phase clouds, 129, 39–65,  
766 <https://doi.org/https://doi.org/10.1256/qj.01.204>, 2003.
- 767 Letcher, T., Cotton, W.R., 2014. The effect of pollution aerosol on wintertime orographic  
768 precipitation in the Colorado Rockies using a simplified emissions scheme to predict CCN  
769 concentrations, *J. Appl. Meteorol. Climatol.* 53 (4), 859–872.
- 770 Levin, E. J. T., DeMott, P. J., Suski, K. J., Boose, Y., Hill, T. C. J., McCluskey, C. S., Schill, G.  
771 P., Rocci, K., Al-Mashat, H., Kristensen, L. J., Cornwell, G., Prather, K., Tomlinson, J.,  
772 Mei, F., Hubbe, J., Pekour, M., Sullivan, R., Leung, L. R., and Kreidenweis, S. M.:  
773 Characteristics of Ice Nucleating Particles in and Around California Winter Storms, 124,  
774 11530–11551, <https://doi.org/10.1029/2019JD030831>, 2019.
- 775 Lin, Y., Fan, J., Jeong, J.-H., Zhang, Y., Homeyer, C. R., and Wang, J.: Urbanization-Induced  
776 Land and Aerosol Impacts on Storm Propagation and Hail Characteristics, 78, 925–947,  
777 <https://doi.org/10.1175/jas-d-20-0106.1>, 2020.
- 778 Martin, A. C., Cornwell, G., Beall, C. M., Cannon, F., Reilly, S., Schaap, B., Lucero, D.,  
779 Creamean, J., Martin Ralph, F., Mix, H. T., and Prather, K.: Contrasting local and long-  
780 range-transported warm ice-nucleating particles during an atmospheric river in coastal  
781 California, USA, 19, 4193–4210, <https://doi.org/10.5194/acp-19-4193-2019>, 2019.
- 782 Matthews, A., F. Mei, and J. Comstock (2015), Water content monitor (WCM-2000), ARM  
783 Airborne Facility (AAF). Atmospheric Radiation Measurement (ARM) Climate Research  
784 Facility Data Archive, data set acquired 27 Jan 2015 and accessed 10 Jan 2016.
- 785 McCluskey, C. S., Ovadnevaite, J., Rinaldi, M., Atkinson, J., Belosi, F., Ceburnis, D., Marullo,  
786 S., Hill, T. C. J., Lohmann, U., Kanji, Z. A., O’Dowd, C., Kreidenweis, S. M., and DeMott,  
787 P. J.: Marine and Terrestrial Organic Ice-Nucleating Particles in Pristine Marine to  
788 Continentally Influenced Northeast Atlantic Air Masses, 123, 6196–6212,  
789 <https://doi.org/10.1029/2017JD028033>, 2018a.





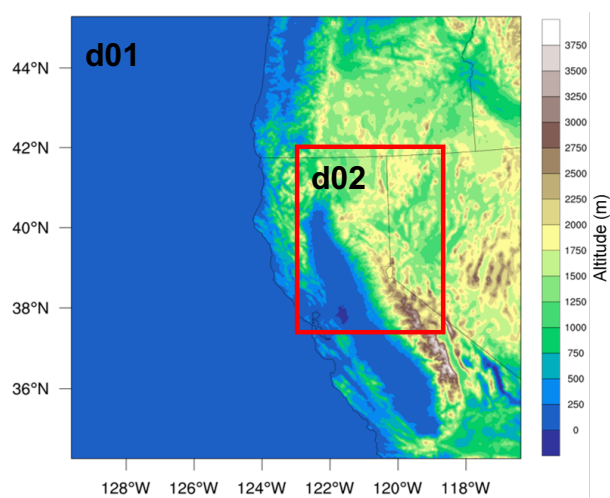
- 790 McCluskey, C. S., Hill, T. C. J., Humphries, R. S., Rauker, A. M., Moreau, S., Stratton, P. G.,  
791 Chambers, S. D., Williams, A. G., McRobert, I., Ward, J., Keywood, M. D., Harnwell, J.,  
792 Ponsonby, W., Loh, Z. M., Krummel, P. B., Protat, A., Kreidenweis, S. M., and DeMott, P.  
793 J.: Observations of Ice Nucleating Particles Over Southern Ocean Waters, 45, 11,989–  
794 11,997, <https://doi.org/10.1029/2018GL079981>, 2018b.
- 795 Mellor, G. L. and Yamada, T.: Development of a turbulence closure model for geophysical fluid  
796 problems, 20, 851–875, <https://doi.org/10.1029/RG020i004p00851>, 1982.
- 797 Meyers, M. P., DeMott, P. J., and Cotton, W. R.: New Primary Ice-Nucleation Parameterizations  
798 in an Explicit Cloud Model, 31, 708–721, [https://doi.org/10.1175/1520-  
799 0450\(1992\)031<0708:NPINPI>2.0.CO;2](https://doi.org/10.1175/1520-0450(1992)031<0708:NPINPI>2.0.CO;2), 1992.
- 800 Muhlbauer, A., Lohmann, U.: Sensitivity studies of the role of aerosols in warm- phase  
801 orographic precipitation in different dynamical flow regimes. *J. Atmos. Sci.* 65 (8), 2522–  
802 2542, 2008.
- 803 Muhlbauer, A. and Lohmann, U.: Sensitivity studies of aerosol-cloud interactions in mixed-  
804 phase orographic precipitation, 66, 2517–2538, <https://doi.org/10.1175/2009JAS3001.1>,  
805 2009.
- 806 Murray, B. J., O’Sullivan, D., Atkinson, J. D., and Webb, M. E.: Ice nucleation by particles  
807 immersed in supercooled cloud droplets., 41, 6519–6554,  
808 <https://doi.org/10.1039/c2cs35200a>, 2012.
- 809 Niemand, M., Möhler, O., Vogel, B., Vogel, H., Hoose, C., Connolly, P., Klein, H., Bingemer,  
810 H., DeMott, P., Skrotzki, J., and Leisner, T.: A Particle-Surface-Area-Based  
811 Parameterization of Immersion Freezing on Desert Dust Particles, 69, 3077–3092,  
812 <https://doi.org/10.1175/jas-d-11-0249.1>, 2012.
- 813 Ralph, F. M., Prather, K. A., Cayan, D., Spackman, J. R., DeMott, P., Dettinger, M., Fairall, C.,  
814 Leung, R., Rosenfeld, D., Rutledge, S., Waliser, D., White, A. B., Cordeira, J., Martin, A.,  
815 Helly, J., and Intrieri, J.: CalWater Field Studies Designed to Quantify the Roles of  
816 Atmospheric Rivers and Aerosols in Modulating U.S. West Coast Precipitation in a  
817 Changing Climate, 97, 1209–1228, <https://doi.org/10.1175/bams-d-14-00043.1>, 2016.
- 818 Reynolds, D. W.: A Report on Winter Snowpack-Augmentation, 69, 1290–1300,  
819 [https://doi.org/10.1175/1520-0477\(1988\)069<1290:AROWSA>2.0.CO;2](https://doi.org/10.1175/1520-0477(1988)069<1290:AROWSA>2.0.CO;2), 1988.
- 820 Rosenfeld, D., Chemke, R., Demott, P., Sullivan, R. C., Rasmussen, R., McDonough, F.,  
821 Comstock, J., Schmid, B., Tomlinson, J., Jonsson, H., Suski, K., Cazorla, A., and Prather,  
822 K.: The common occurrence of highly supercooled drizzle and rain near the coastal regions  
823 of the western United States, 118, 9819–9833, <https://doi.org/10.1002/jgrd.50529>, 2013.
- 824 Saleeby, S.M., Cotton, W.R., Fuller, J.D.: The cumulative impact of cloud droplet nucleating  
825 aerosols on orographic snowfall in Colorado. *J. Appl. Meteorol. Climatol.* 50 (3), 604–625,  
826 2011.
- 827 Saleeby, S.M., Cotton, W.R., Lowenthal, D., Messina, J.: Aerosol impacts on the microphysical  
828 growth processes of orographic snowfall. *J. Appl. Meteorol. Climatol.* 52 (4), 834–852,  
829 2013.
- 830 Schmid, B., Tomlinson, J. M., Hubbe, J. M., Comstock, J. M., Mei, F., Chand, D., Pekour, M. S.,  
831 Kluzek, C. D., Andrews, E., Biraud, S. C., and McFarquhar, G. M.: The DOE arm aerial  
832 facility, 95, 723–742, <https://doi.org/10.1175/BAMS-D-13-00040.1>, 2014.
- 833 Shaw, W. J., Jerry Allwine, K., Fritz, B. G., Rutz, F. C., Rishel, J. P., and Chapman, E. G.: An  
834 evaluation of the wind erosion module in DUSTRAN, 42, 1907–1921,  
835 <https://doi.org/10.1016/j.atmosenv.2007.11.022>, 2008.



- 836 Thompson, D. R., McCubbin, I., Gao, B. C., Green, R. O., Matthews, A. A., Mei, F., Meyer, K.  
837 G., Platnick, S., Schmid, B., Tomlinson, J., and Wilcox, E.: Measuring cloud  
838 thermodynamic phase with shortwave infrared imaging spectroscopy, 121, 9174–9190,  
839 <https://doi.org/10.1002/2016JD024999>, 2016.
- 840 Uno, I., Eguchi, K., Yumimoto, K., Takemura, T., Shimizu, A., Uematsu, M., Liu, Z., Wang, Z.,  
841 Hara, Y., and Sugimoto, N.: Asian dust transported one full circuit around the globe, 2, 557–  
842 560, <https://doi.org/10.1038/ngeo583>, 2009.
- 843 Vali, G., DeMott, P. J., Möhler, O., and Whale, T. F.: Technical Note: A proposal for ice  
844 nucleation terminology, 15, 10263–10270, <https://doi.org/10.5194/acp-15-10263-2015>,  
845 2015.
- 846 Vergara-Temprado, J., Murray, B. J., Wilson, T. W., O’Sullivan, D., Browse, J., Pringle, K. J.,  
847 Ardon-Dryer, K., Bertram, A. K., Burrows, S. M., Ceburnis, D., Demott, P. J., Mason, R.  
848 H., O’Dowd, C. D., Rinaldi, M., and Carslaw, K. S.: Contribution of feldspar and marine  
849 organic aerosols to global ice nucleating particle concentrations, 17, 3637–3658,  
850 <https://doi.org/10.5194/acp-17-3637-2017>, 2017.
- 851 Xiao, H., Yin, Y., Jin, L., Chen, Q., and Chen, J.: Simulation of the effects of aerosol on mixed-  
852 phase orographic clouds using the WRF model with a detailed bin microphysics scheme,  
853 120, 8345–8358, <https://doi.org/10.1002/2014JD022988>, 2015.
- 854 Yang, Y., Sun, J., Zhu, Y., and Zhang, T.: Examination of the impacts of ice nuclei aerosol  
855 particles on microphysics, precipitation and electrification in a 1.5D aerosol-cloud bin  
856 model, 140, 105440, <https://doi.org/10.1016/j.jaerosci.2019.105440>, 2020.
- 857 Yun, Y. and Penner, J. E.: An evaluation of the potential radiative forcing and climatic impact of  
858 marine organic aerosols as heterogeneous ice nuclei, 40, 4121–4126,  
859 <https://doi.org/10.1002/grl.50794>, 2013.
- 860 Zaveri, R. A., Easter, R. C., Fast, J. D., and Peters, L. K.: Model for Simulating Aerosol  
861 Interactions and Chemistry (MOSAIC), 113,  
862 <https://doi.org/10.1029/2007jd008782>, 2008.
- 863 Zhang, Y., Fan, J., Li, Z., and Rosenfeld, D.: Impacts of Cloud Microphysics Parameterizations  
864 on Simulated Aerosol–Cloud–Interactions for Deep Convective Clouds over Houston, 1–46,  
865 <https://doi.org/10.5194/acp-2020-372>, 2020.
- 866 Zhao, C., Chen, S., Leung, L. R., Qian, Y., Kok, J. F., Zaveri, R. A., and Huang, J.: Uncertainty  
867 in modeling dust mass balance and radiative forcing from size parameterization, *Atmos.*  
868 *Chem. Phys.*, 13, 10733–10753, <https://doi.org/10.5194/acp-13-10733-2013>, 2013  
869  
870



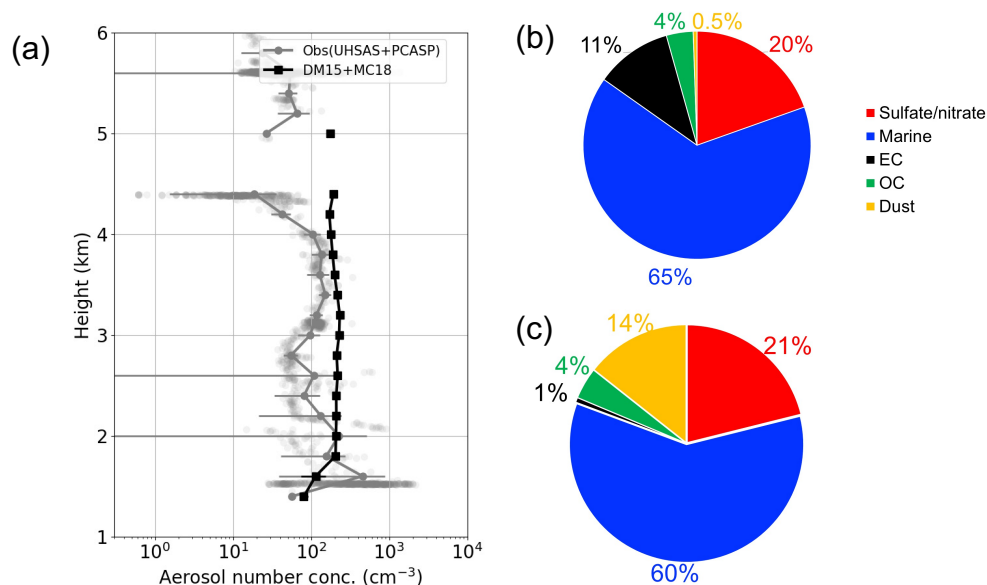
871 **Figures**



872

873 **Figure 1.** Two nested simulation domains: d01 and d02 centering over California. The color  
874 shading denotes the terrain elevation.

875

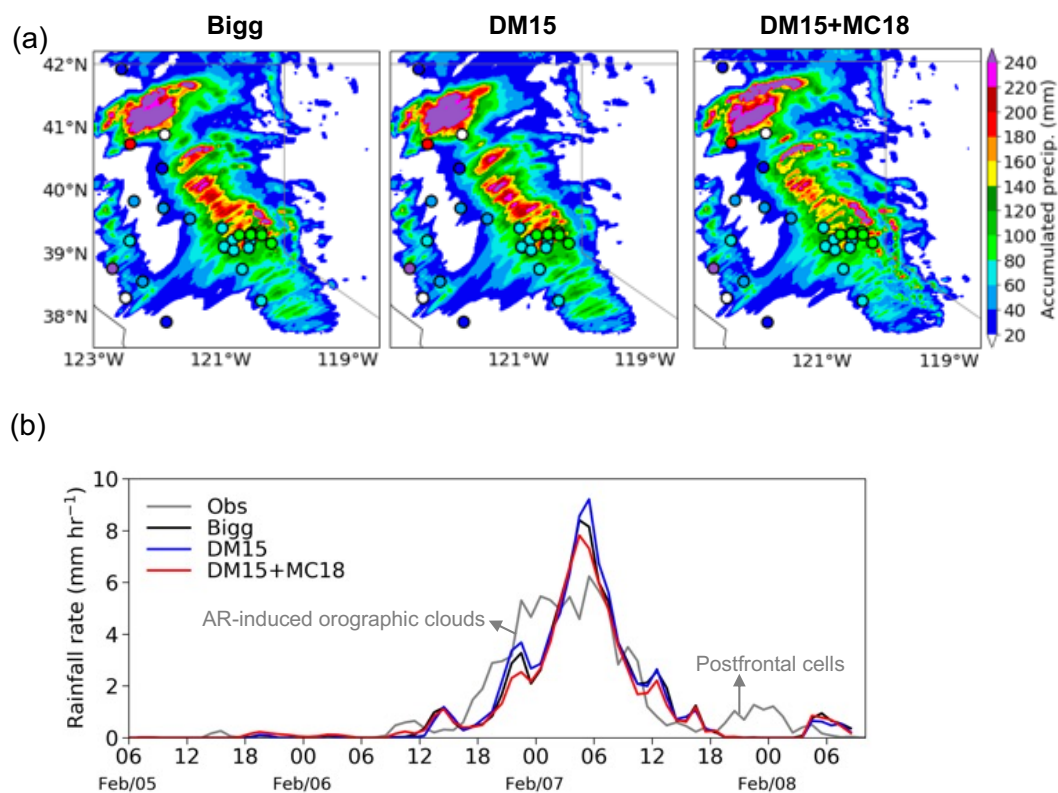


876

877 **Figure 2.** (a) Vertical distributions of aerosol number concentrations from aircraft observations  
878 (Obs, grey) and DM15+MC18 (black) for particles with a dry diameter over a range of 0.067–3  
879  $\mu\text{m}$ , (b) mean fractional number contributions of aerosol classifications based on measurements  
880 of single-particle mass spectra of aerosols and cloud particle residuals reported in Levin et al.  
881 (2019), and (c) mean fractional mass contributions of aerosols in DM15+MC18 (number  
882 concentration for each aerosol component is not predicted by WRF-Chem). The aerosol number  
883 concentration from aircraft observations in (a) consists of both measurements from UHSAS and  
884 PCASP. The modeled data in (a) and (c) are sampled along the aircraft route on 7 February 2015.

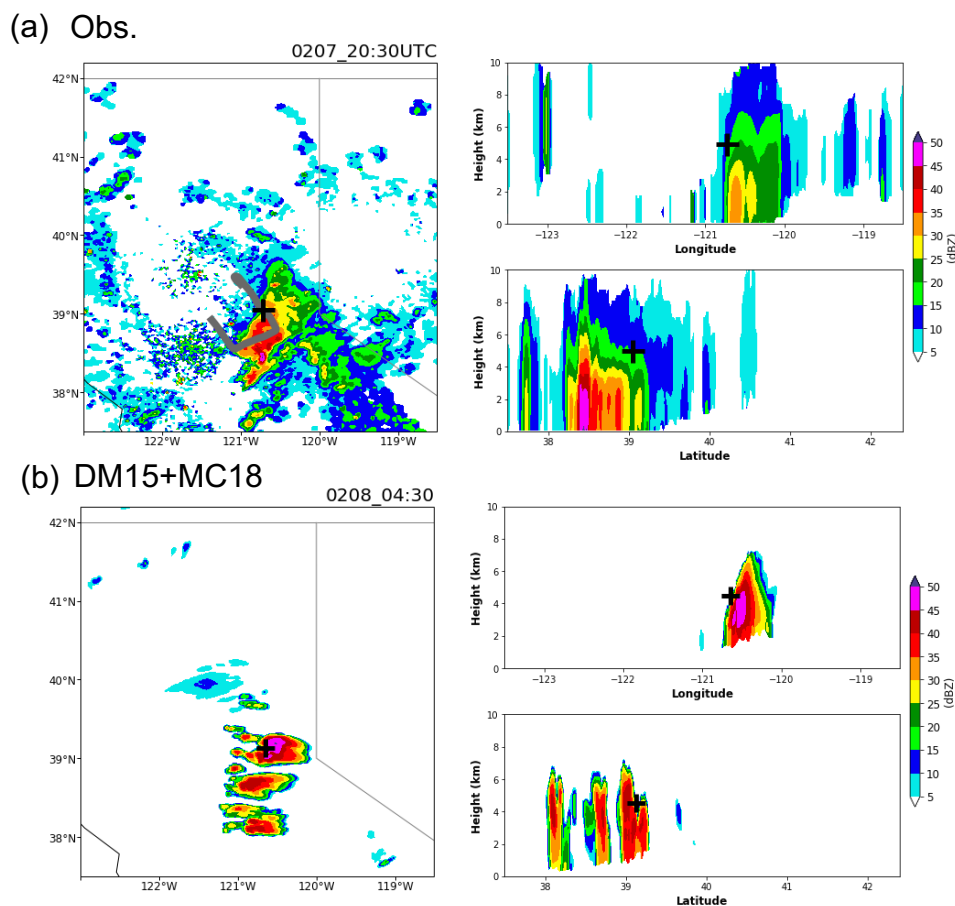
885

886

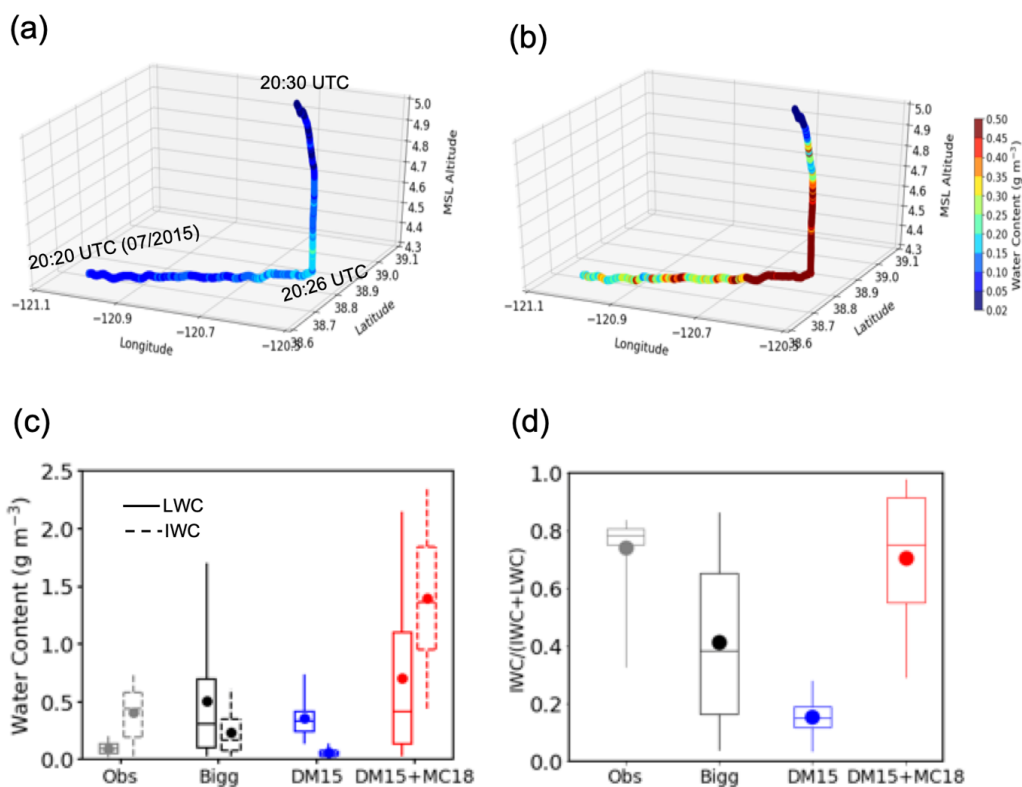


887

888 **Figure 3.** (a) Spatial distributions of accumulated precipitation during the AR event (06:00 UTC  
889 5– 09:00 UTC 8 February). The color shading is for simulations and the circles denote the rain  
890 gauge measurements provided by NOAA’s Physical Sciences Laboratory. (b) Time series of  
891 precipitation rates during the entire AR event for rain gauge observations (grey), and the  
892 simulations of Bigg (black), DM15 (blue), and DM15+MC18 (red). The precipitation rates are  
893 averaged over all the rain gauge sites shown in (a) for both observations and simulations. The  
894 observed AR-induced orographic clouds and postfrontal cells are marked in (b).

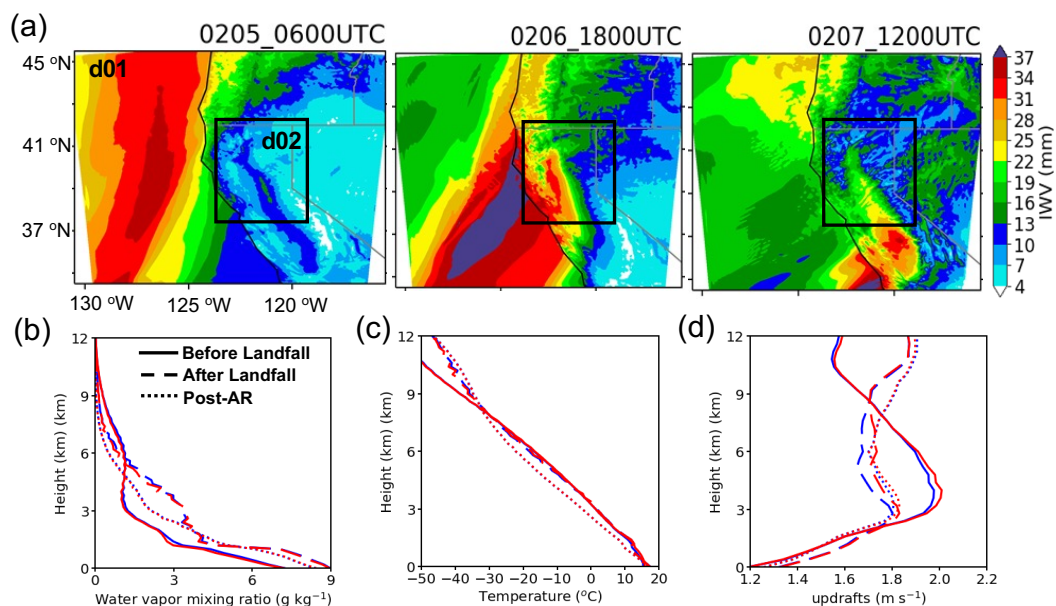


895  
896 **Figure 4.** (a) Composite reflectivity of NEXRAD for the postfrontal clouds that the G-1 aircraft  
897 sampled, (b) composite reflectivity from the simulation of DM15+MC18 for the postfrontal  
898 clouds. The observation and simulation are compared at the peak reflectivity time which is 20:30  
899 UTC 7 February for the observed clouds and 04:30 UTC 8 February for the simulated clouds.  
900 The black crosses in the left two panels denote the positions where the longitude-height and  
901 latitude-height cross-sections in the right panels are plotted. The grey line in the left panel of (a)  
902 shows the flight track of the G-1 aircraft.



903  
904

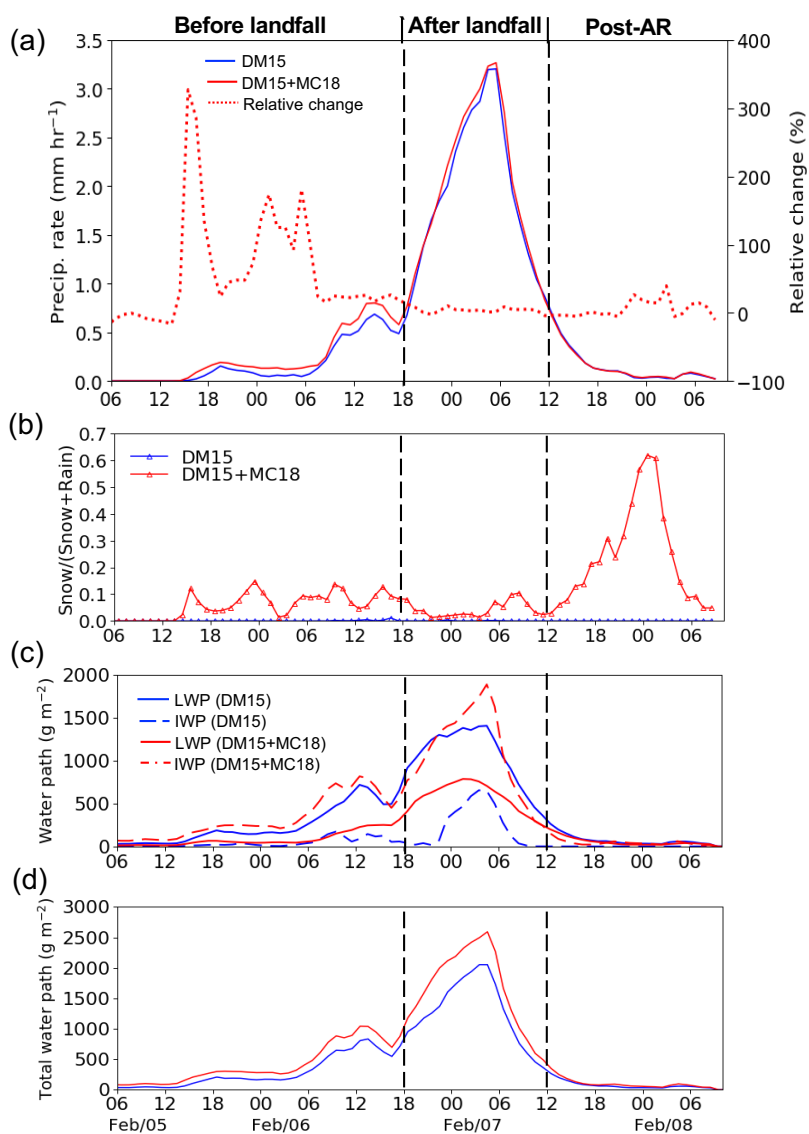
905 **Figure 5.** Comparisons of the simulations with aircraft observations. The observed (a) LWC and  
906 (b) IWC along the flight track during 20:20 – 20:30 on 7 February when the aircraft flew through  
907 the mixed-phase regime of the postfrontal clouds. (c) LWC (solid) and IWC (dashed) and (d) the  
908 glaciation ratios of  $\text{IWC}/(\text{IWC}+\text{LWC})$  from the aircraft measurements (Obs, grey) and  
909 simulations of Bigg (black), DM15 (blue), and DM15+MC18 (red). The boxes show the 25th,  
910 median (horizontal lines in the box), and 75th percentiles of the data. The upper and lower  
911 whiskers show the 95<sup>th</sup> and 5<sup>th</sup> percentiles, respectively. The mean values are denoted by circles.



912

913 **Figure 6.** (a) Evolution of integrated water vapor (IWV) at 06:00 UTC 5 February (before AR  
914 landfall), 18:00 UTC 6 February (after AR landfall), and 12:00 UTC 7 February (post-AR). The  
915 black box (i.e., d02) in (a) is the domain of this study with the 5 lateral boundary grids excluded  
916 for analysis at each side. (b-d) show the mean vertical profiles of (b) water vapor mixing ratio,  
917 (c) temperature, and (d) updraft velocity at the three AR stages, i.e., before (solid lines) and after  
918 (dashed lines) AR landfall and post-AR stages (dotted lines), for the simulations of DM15 (blue)  
919 and DM15+MC18 (red). The water vapor mixing ratio and temperature are averaged for cloud-  
920 free grids, and updraft velocity is averaged over the grids with a vertical velocity greater than 1  
921 m s<sup>-1</sup>.

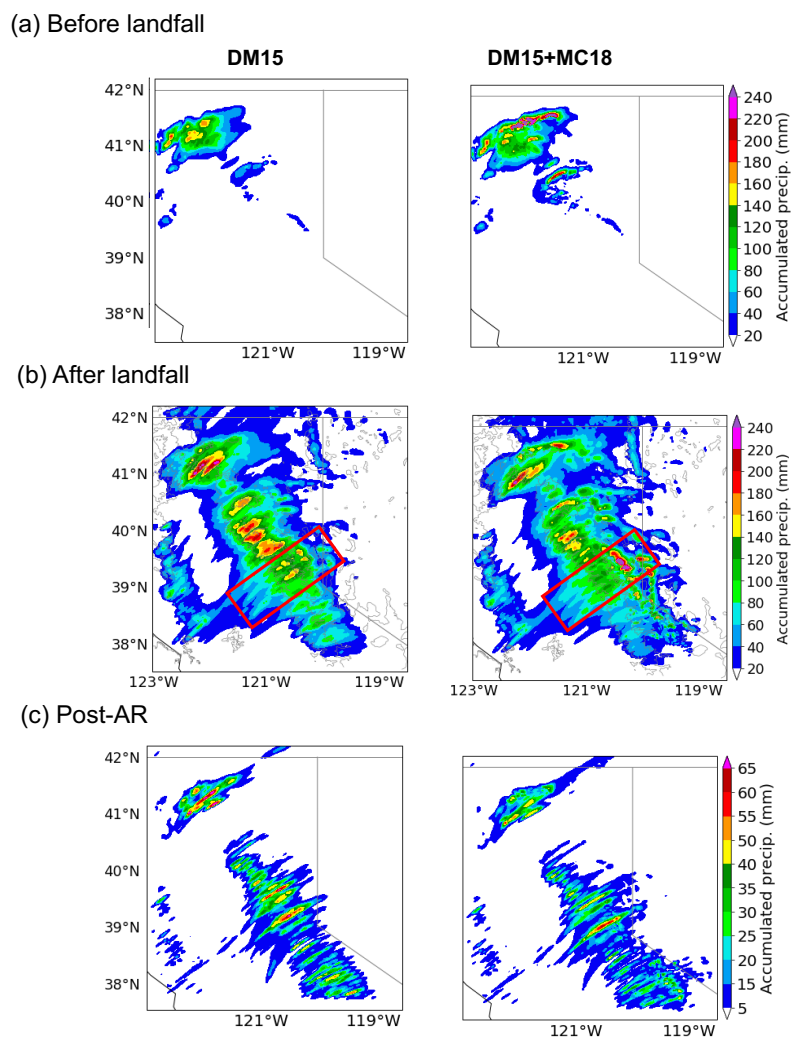




922

923 **Figure 7.** Time series of (a) precipitation rate (solid lines, left y-axis), (b) ratio of snow  
924 precipitation (i.e., snow/(snow+rain) in mass mixing ratio) at the lowest model level, (c) LWP  
925 (solid) and IWP (dashed) for DM15 (blue) and DM15+MC18 (red), and (d) total condensate  
926 water path (TWP). The relative changes in precipitation rate from DM15 to DM15+MC18 are  
927 shown in the red dotted line in (a) with values shown on the right y-axis. The vertical dashed  
928 lines divide the three AR stages.

929



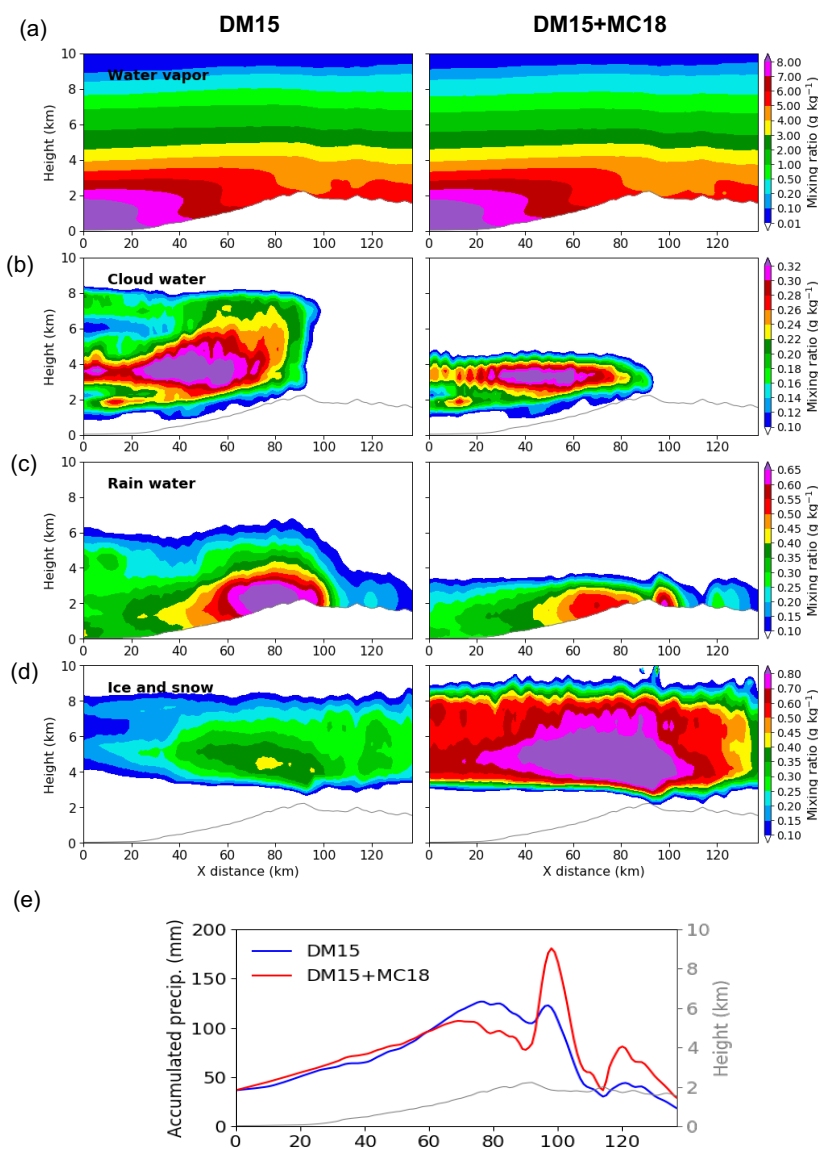
930

931 **Figure 8.** Spatial distribution of accumulated precipitation during the stages of (a) before AR  
932 landfall, (b) after AR landfall, and (c) post-AR in DM15 (left) and DM15+MC18 (right). The  
933 parallelograms marked in (b) denotes the area for the east-west cross-section analysis shown in  
934 Figure 9.

935

936

937



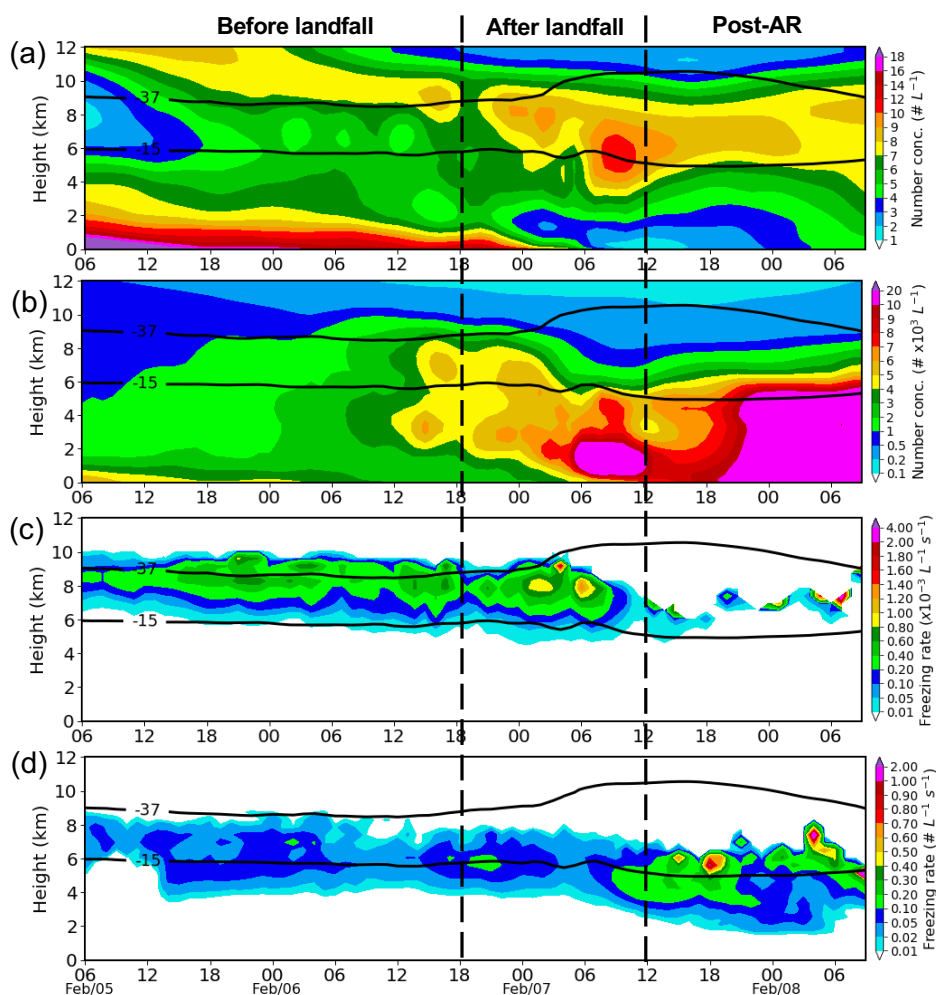
938

939

940 **Figure 9.** Mean mixing ratios of (a) water vapor, (b) cloud water, (c) rainwater, (d) ice + snow,  
941 and (e) surface precipitation at the stage after AR landfall in DM15 and DM15+MC18. The  
942 vertical cross-sections are averaged over the red boxes marked in Fig. 8b and the entire stage.



943

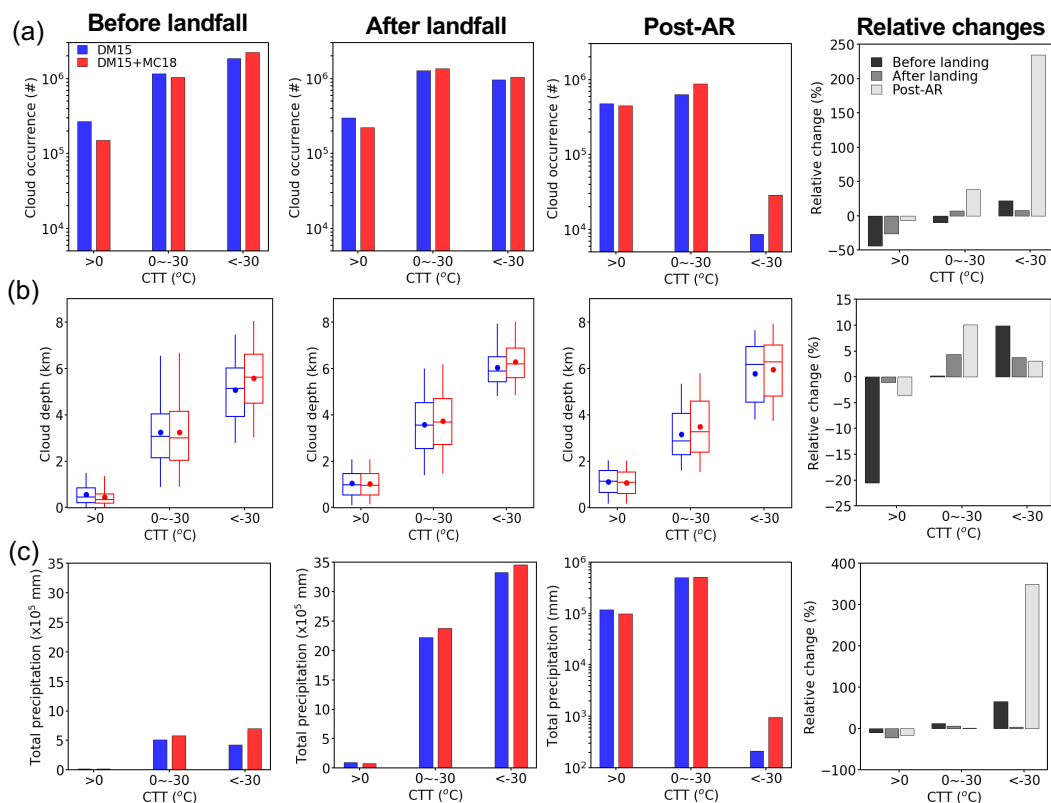


944

945 **Figure 10.** Time-height cross-sections of (a) dust particle ( $>0.5 \mu\text{m}$ ) number concentration, (b)  
946 marine aerosol number concentration, (c) the freezing rate in DM15, and (d) the freezing rate in  
947 DM15+MC18. The number concentrations in (a) and (b) are derived from their corresponding  
948 mass mixing ratios under the clear-sky condition only. The freezing rates in (b) and (d) are the  
949 ice nucleation rates via immersion freezing at  $T > -37 \text{ }^\circ\text{C}$  and the drop homogenous freezing  
950 rates at  $T < -37 \text{ }^\circ\text{C}$ , and the values are for cloudy-points only. The black contour lines in each  
951 panel mark the temperature levels of  $-15$  and  $-37 \text{ }^\circ\text{C}$ , representing the efficient immersion  
952 freezing temperature in DM15+MC18 and the homogeneous freezing temperature in the model,  
953 respectively.

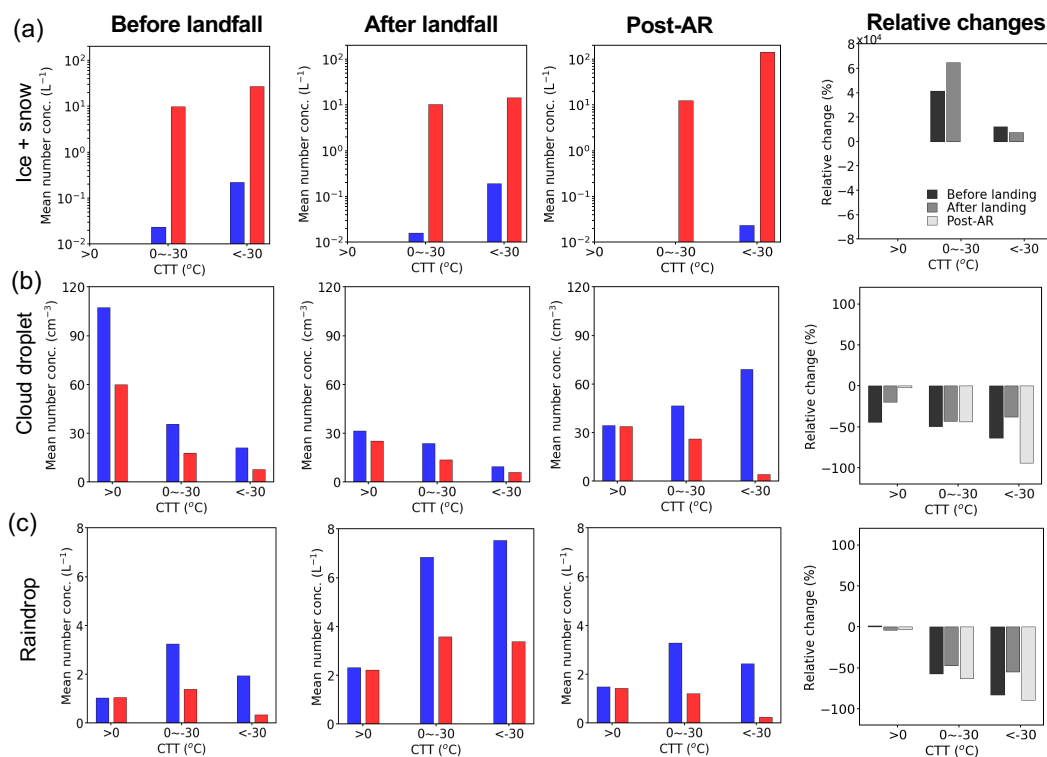


954



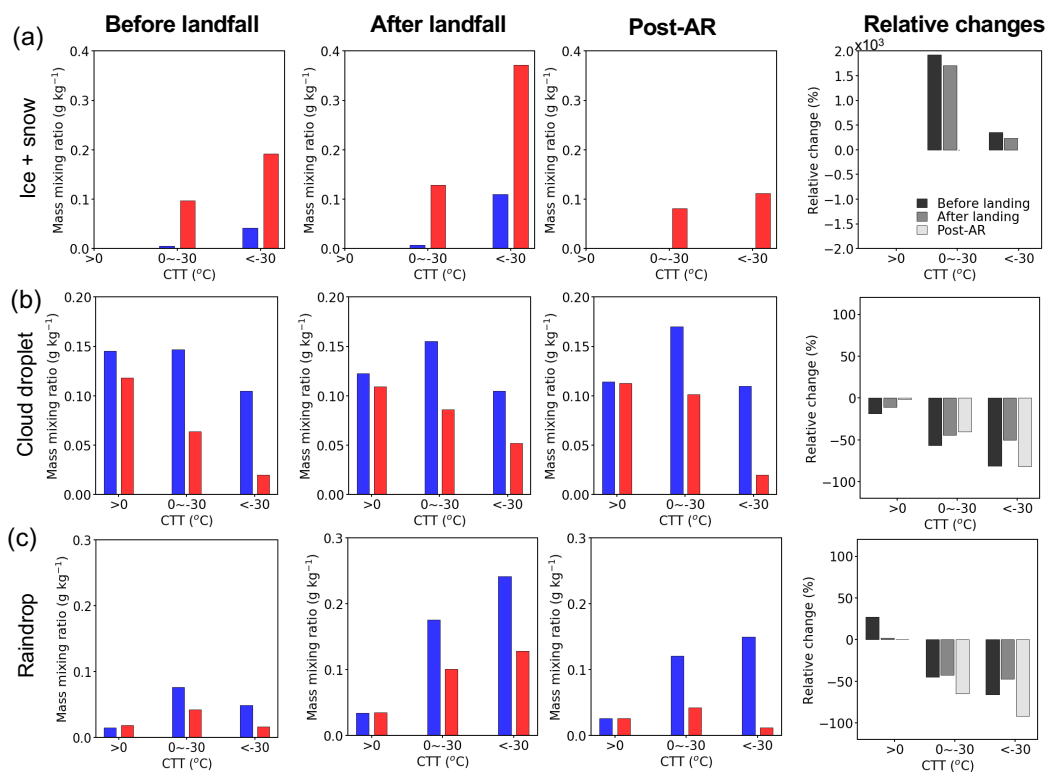
955

956 **Figure 11.** (a) cloud occurrences, (b) cloud depth, and (c) total precipitation for three cloud  
 957 regimes in DM15 (blue) and DM15+MC18 (red) at three AR stages from left to right: before AR  
 958 landfall, after AR landfall, post-AR. The last column shows the relative changes caused by the  
 959 marine INP effect, which are calculated as  $[(DM15+MC18) - DM15]/DM15 * 100\%$ . Note that  
 960 the total precipitation at the post-AR stage uses a log scale for the y-axis. The box-whisker plots  
 961 follow the description in Figure 5c.



962

963 **Figure 12.** Hydrometeor number concentrations and their relative changes in three cloud regimes  
 964 in DM15 (blue) and DM15+MC18 (red) at the three AR stages for (a) ice particles (sum of ice  
 965 and snow), (b) cloud droplets, and (c) raindrops. The last column shows the relative changes  
 966 caused by the marine INP effect, which are calculated as  $[(DM15+MC18) -$   
 967  $DM15]/DM15*100\%$ . Since ice particles are very limited at the post-AR stage in DM15, the  
 968 percentage changes of ice particles from DM15 to DM15+MC18 are huge numbers that are  
 969 omitted from the plots.



970

971 **Figure 13.** Same as Figure 12, except for the mass mixing ratios of (a) ice particles (sum of ice  
 972 and snow), (b) cloud droplets, and (c) raindrops.

973

974

975

976

977

978

979

980

981



982

983 **Table 1.** The changes in total precipitation, total condensate water path (TWP), liquid water path  
 984 (LWP), and ice water path (IWP), and cloud fractions (CF), net cloud radiative forcing (CRF) at  
 985 TOA from DM15 to DM15+MC18 (i.e., the marine INP effect), as well as the glaciation ratio,  
 986 i.e.,  $IWC/(LWC+IWC)$ , and the ratios of snow precipitation, i.e.,  $snow/(rain+snow)$  in mass  
 987 mixing ratio at the lowest model level from DM15 to DM15+MC18, at the three AR stages. The  
 988 percentage changes are calculated following  $((DM15+MC18) - DM15)/DM15 * 100$ .

989

AR stages		Before landfall	After landfall	Post-AR
Total precipitation		36%	4%	-1%
TWP		45%	29%	35%
LWP		-66%	-46%	-26%
IWP		8 times	5 times	440 times
CF		5%	4%	20%
Net CRF at TOA		15%	13%	10%
$IWC/(LWC+IWC)$	DM15	0.14	0.16	0.001
	DM15+MC18	0.74	0.59	0.36
$Snow/(Rain+Snow)$	DM15	0.002	0.001	<0.001
	DM15+MC18	0.085	0.042	0.131

990

991





992 **Table 2.** The domain-mean mass rates of deposition and riming in the mixed-phase and deep  
993 cloud regimes in DM15 and DM15+MC18 at the three AR stages.

AR stages		Before landfall		After landfall		Post-AR	
		Mixed-phase clouds	Deep clouds	Mixed-phase clouds	Deep clouds	Mixed-phase clouds	Deep clouds
Deposition ( $\text{mg kg}^{-1} \text{ h}^{-1}$ )	DM15	44	171	81	388	7	8
	DM15+MC18	846	780	1128	1397	781	1013
Riming ( $\text{mg kg}^{-1} \text{ h}^{-1}$ )	DM15	27	89	57	297	25	34
	DM15+MC18	377	228	575	858	505	361

994

995